Morphology of a thermally stable small molecule OPV blend comprising a liquid crystalline donor and fullerene acceptor

Alexander J. Bourque,[1] Sebastian Engmann,[2,1] Allison Fuster,[1] Chad R. Snyder,*[1] Lee J. Richter,[1] Paul B. Geraghty,[3] David J. Jones[3]

[1]*Materials Science and Engineering Division, National Institute of Standards and Technology, Gaithersburg, MD 20899, USA.*

[2]*Theiss Research, La Jolla, California 92037*

[3]*School of Chemistry, Bio21 Institute, The University of Melbourne, 30 Flemington Road, Parkville, Victoria 3010, Australia.*

Abstract

Recently organic photovoltaic (OPV) devices comprising the small-molecule liquid-crystalline donor, benzodithiophene-quaterthiophene-rhodanine (BQR), and fullerene acceptor, [6,6]-phenyl C_{71} butyric acid methyl ester ($PC_{71}BM$), were demonstrated to achieve high performance when thermally processed, avoiding the need for slow-drying solvent additives or complex solvent-vapor annealing post-processing. In this investigation we explore the impact of thermal processing on thin film blends of BQR and $PC_{71}BM$ using differential scanning calorimetry (DSC), *in situ* grazing incidence X-ray scattering (GISAXS, GIWAXS), and photoluminescence spectroscopy (PL) to correlate thermal behavior with morphological changes and photoactivity. We develop a phase diagram of the crystalline and liquid crystalline transitions in BQR and the related high performing electron donor material, benzodithiophene-terthiophene-rhodanine (BTR), and are able to predict phase transitions using Flory-Huggins theory, including suppression of liquid crystalline phase formation in the presence of $PC_{71}BM$. Further DSC measurements demonstrate the superior thermal stability of $PC_{71}BM$ blends with BQR over blends with BTR. OPV devices with the BQR:$PC_{71}BM$ active layer were prepared using the blade-coated deposition technique and exhibit optimal device performance when annealed at 120 °C for 5 min. The characteristic

acceptor/donor domain size in an as-cast BQR:$PC_{71}BM$ film, estimated from GISAXS, was about 60 nm which is sufficient for exciton separation. Domain purity was enhanced by annealing at temperatures above ≈ 80 °C. Annealing at temperatures above ≈ 120 °C resulted in over-coarsening of the acceptor/donor-rich phases to domain sizes beyond 80 nm and reduced performance.

Introduction

Organic photovoltaics (OPVs) remain an attractive option for harvesting solar power to generate electricity. Compared to conventional solid-state photovoltaics, organic solar cells promise low-cost, scalable production with earth abundant, nontoxic starting materials. The most likely route towards commercial viability is through solution processing of OPV devices via roll-to-roll printing.[1–3] One of the primary challenges in printing OPVs is the need for thick (> 200 nm) active layer films to be produced free of pinhole defects with good reproducibility at high printing speeds. Unfortunately, the majority of successful OPV blends optimize at thicknesses of roughly 100 nm; few have achieved high photovoltaic performance with active layers over 200 nm.[4–8] Another general challenge for OPVs is batch-to-batch variability exhibited by functional materials of the device. Traditionally, polymers have been used as the electron donor material in OPVs; however, polymer production at scale often lacks the necessary control over purity and dispersity of molar masses to reliably reproduce performance. Small molecule donors, which historically have been outperformed by polymer donors, do not suffer the same reproducibility issues as they can be produced with high purity and discrete control over the molecular architecture. Recent advances in molecular engineering have pushed small-molecule based OPVs towards competitive performance with polymer based devices.[9] The BXR series, shown in Figure 1, is a particularly

promising series of small molecule donors for OPV devices exhibiting high performance in thick active layers. Spun-cast blends of BTR, BQR (benzodithiophene-quaterthiophene-rhodanine), or BPR (benzodithiophene-quinquethiophene-rhodanine) with $PC_{71}BM$ can be post-processed via solvent vapor annealing (SVA) to achieve power conversion efficiencies (PCE) > 8.5 % with film thicknesses > 200 nm.[10]

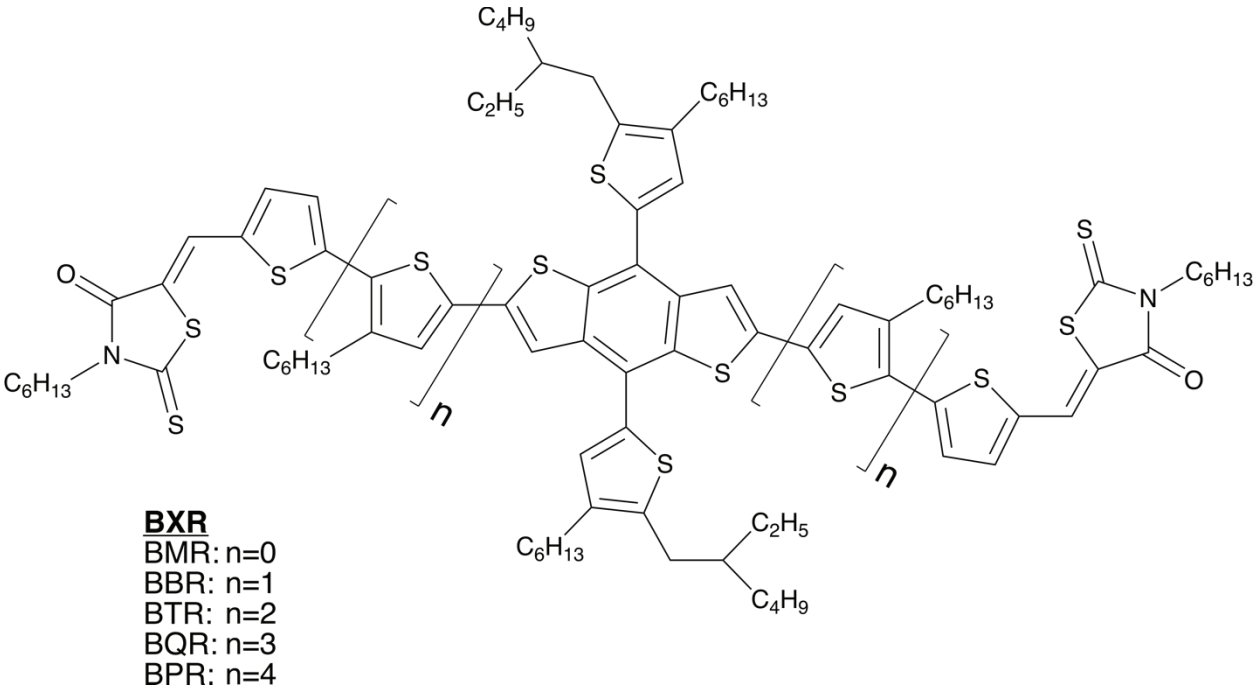

Figure 1. Chemical structures of materials among the BXR series.

For successful high throughput production, photoactive thin films must withstand elevated temperatures that accompany the device manufacturing process, including rapid film drying at temperatures > 80 °C and selective thermal annealing of the layers which make up the final OPV device. The typical active layer morphology, however, comprises a non-equilibrium mixture of

materials forming a co-continuous percolating network. This bulk heterojunction (BHJ) morphology maximizes interfacial area between donor- and acceptor-rich phases resulting in efficient charge generation. Elevated temperatures can drastically modify the metastable active layer morphology, either improving device performance or yielding catastrophic changes. Polymer:fullerene based bulk heterojunction blends are particularly susceptible to rapid coarsening of domains due to fullerene aggregation and subsequent crystal growth if annealed above the blend's glass transition temperature, T_g.[11] By engineering materials with a higher T_g, one can prevent structural rearrangement at elevated temperatures as was shown with MDMO-PPV: $PC_{61}BM$ solar cells.[12,13] Annealing at 110 °C resulted in rapid loss of performance for devices containing a low T_g MDMO-PPV polymer ($T_g \approx 50$ °C), but strongly reduced rates of fullerene crystal formation and performance loss were obtained using a high T_g variant ($T_g \approx 138$ °C) of the MDMO-PPV polymer. Blends containing a crystallizable donor polymer and a fullerene are more robust to thermal annealing due to the presence of immobile crystallites that inhibit fullerene mobility. Such is the case for P3HT:$PC_{61}BM$ blends which exhibit stable OPV performance when annealed for ≈ 10 min at 150 °C,[14] well above the reported glass transition temperature for P3HT, $T_g \approx 12$ °C.[15] Annealing actually improves performance in the P3HT: $PC_{61}BM$ system due to beneficial ordering of the P3HT domains. The robustness to thermal processing is a consequence of polymer chain topology and molecular entanglements that limit the growth of polymer crystallites. Conversely, OPV devices with crystallizable small molecules are more sensitive to thermal processing because the molecules lack strong diffusive barriers. Thermal annealing can result in overgrowth of crystalline donor regions that degrades device performance. Donor materials among the BXR series exhibit significant variability in performance when thermally annealed. Only BQR:$PC_{71}BM$ devices achieve parity in performance (PCE > 8.5 %) via thermal

annealing (TA) compared to post-treatment with SVA.[10] The thermal behavior within the BXR series was explored using differential scanning calorimetry (DSC) and UV-Vis spectroscopy by Geraghty et al.[10] It was found that, like BTR,[4] BQR exhibited multiple liquid crystalline transitions upon cooling. However, device annealing temperatures did not reach above the melting temperature for the reported liquid crystalline transitions in either blend so the unique thermal stability of BQR was not fully understood.

Here we report *in situ* characterization of the BQR:$PC_{71}BM$ system to investigate its unique thermal stability. Using DSC, we examine the thermal behavior of BQR and BTR in the presence of increasing amounts of $PC_{71}BM$. We find that the robustness of BQR devices to thermal annealing compared to BTR devices is governed by differences in $PC_{71}BM$ mobility in the blended systems. *In situ* grazing incidence wide angle X-ray scattering (GIWAXS) measurements of the BQR:$PC_{71}BM$ system subjected to the same thermal processing scheme from DSC were taken to correlate morphological changes with their signatures from calorimetry. Similarly, *in situ* grazing incidence small angle X-ray scattering (GISAXS) was used to track nanometer scale morphological changes during thermal annealing. *In situ* photo-luminescence spectroscopy of the device relevant BQR:$PC_{71}BM$ films corroborates nanoscale segregation of donor- and acceptor-rich domains at elevated temperatures. Finally, we report the performance of blade-coated BQR:$PC_{71}BM$ devices as a function of thermal annealing, allowing identification of the optimal morphology.

Experimental Section

The small molecule donors benzodithiophene-terthiophene-rhodanine (BTR) and benzodithiophene-quaterthiophene-rhodanine (BQR) were synthesized as reported in Geraghty et al.[10] $PC_{71}BM$ was purchased from nano-C and used as received.*

Differential scanning calorimetry (DSC)

DSC was performed on a TA Instruments Q1000 heat flux DSC in TP4 mode. Sample masses between 2 mg to 3 mg were prepared in ultra-light Perkin Elmer HyperDSC aluminum pans by drop casting relevant solutions directly into the pan. Pristine BQR, BTR and $PC_{71}BM$ stock solutions, each with a concentration of 20 mg/mL in chloroform, were prepared for samples among the BQR:$PC_{71}BM$ loading series and BTR:$PC_{71}BM$ loading series. Solutions with the specified donor:acceptor ratio were prepared by blending appropriate volumes of stock solution. Samples were prepared under inert atmosphere atop a hot plate at 50 °C and left to dry for 1 h. Sample pans for the BQR and BTR thermal annealing series were prepared from a 40 mg/mL solution of 50:50 BQR:$PC_{71}BM$ in toluene and a 40 mg/mL solution of 50:50 BTR:$PC_{71}BM$ in chloroform, respectively. Measurements were performed under a dry nitrogen purge of 50 mL/min. Samples among the loading series were heated at 10 °C/min to 215 °C and subsequently cooled to 0 °C at three different cooling rates (10 °C/min, 5 °C/min and 1 °C/min) with a 10 °C/min heating ramp back up to 215 °C following each ramp down. The end of each temperature ramp was followed by a 1 min isothermal hold before proceeding to the next ramp. A duplicate set of samples for the BQR:$PC_{71}BM$ and BTR:$PC_{71}BM$ loading series was prepared to measure $PC_{71}BM$ melting point

* Certain commercial equipment, instruments or materials are identified in this paper in order to specify the experimental procedure adequately. Such identification is not intended to imply recommendation or endorsement by the National Institute of Standards and Technology, nor is it intended to imply the materials or equipment identified are necessarily the best available for the purpose.

depression. These samples were heated at 10 °C/min to 350 °C. Sample pans for the BQR and BTR annealing series were held at the specified annealing temperature on a hot plate under inert atmosphere for 5 min. DSC measurements were performed on the annealed samples using a 10 °C/min heat ramp up to 350 °C.

In situ X-ray scattering

Thin film samples for X-ray measurements were prepared on silicon substrates with a native oxide using a low-angle blade-coater.[16] Solutions for blade-coating were prepared from pristine stock solutions of BQR and $PC_{71}BM$ containing 20 mg of solids per mL toluene. Solutions with the specified mass ratio of BQR and $PC_{71}BM$ were blended in appropriate volumetric amounts. Approximately 20 μL solution was dispensed under the edge of a glass blade held 300 μm above the silicon substrate. The blade was immediately translated over the length of the substrate at a speed of 40 mm/s to generate a film with an approximate thickness of 100 nm. Film thickness was determined by spectroscopic ellipsometry.

X-ray scattering measurements were performed at the Cornell High Energy Synchrotron Source (CHESS) on the D1 beamline with a beam energy of 10.7 keV and beam width of 300 μm. A 2D image detector (Pilatus 2K) was located at a distance of 173 mm from the sample center for GIWAXS measurements and 1850 mm from the sample center for GISAXS measurements. The measurements were performed in ambient air. A flight tube filled with helium gas was used for GISAXS measurements to minimize air scatter. The sample stage temperature was controlled to collect *in situ* thermal annealing measurements. The temperature program was specified to heat

the stage, initially at 30 °C, to 215 °C, cool down to 50 °C, and finally re-heat to 215 °C using a heating/cooling rate of 10 °C/min. The stage was cooled by ambient air thus the temperature on cooling deviated from the programmed 10 °C/min cooling rate over the course of the experiment. The stage temperature was recorded over the course of the experiment for direct analysis. X-ray scattering measurements were collected every 30 s with 3 s of beam exposure on the sample. The sample stage and thus the sample were translated by 0.05 mm normal to the beam path after each integration period to minimize potential beam damage to the film over the course of the measurement. Both GIWAXS and GISAXS data were reduced with the Nika software package.[17]

Solar cell devices

Patterned ITO (≈ 140 nm, 20 Ω/sq.) on glass substrates were purchased from Thin Film Devices. Substrates were scrubbed clean with laboratory detergent and DI water and subsequently sonicated in DI water, acetone and isopropanol, each for 15 minutes. Just before depositing the layers of the device, the substrates were UV-Ozone treated for 10 min. A 30 nm thick layer of PEDOT:PSS (Clevios® P VP Al 4083) was spin-coated at 4000*2π/60 rad/s (4000 RPM) for 60 s and dried at 130 °C for 20 min in air. Devices were quickly moved from the hot plate to a nitrogen glove box where the active layer was blade-coated. The active layer solution (40 mg/mL solution of 50:50 BQR:$PC_{71}BM$ in toluene) was blade-coated as described for thin film X-ray samples. The stage temperature was held at 30 °C during film deposition. For thermally annealed devices, the substrate was placed on a hot plate at the specified annealing temperature for 5 min. The top electrode was thermally evaporated through a shadow mask over the active layer. 15 nm of Ca was deposited followed by 80 nm of Al. The pressure during the evaporation was below 1 x 10^{-4} Pa. The active

area of the finished device, defined by the overlap of the prepatterned ITO and metal top electrode, was 0.04 cm^2. Current density-voltage measurements were made under simulated AM1.5G 100 mW/cm^2 illumination using a Keithley 2600 SMU under argon atmosphere without exposure to air. The OPV device performance was referenced to a KG5 filtered silicon photodiode calibrated by the National Renewable Energy Laboratory.

Photoluminescence (PL) spectroscopy

Thin film samples for photoluminescence spectroscopy were prepared on glass microscope slides using the blade-coating technique. Films were prepared identically to the active layer in the solar cell devices as described above. The films were transferred from the nitrogen environment in which they were prepared to ambient air. *In situ* PL measurements were collected while thermal annealing the substrate. The stage temperature was ramped at 10 °C/min from 30 °C to 180 °C during the measurements. A detailed description of the PL setup and measurement methods are reported elsewhere.[18] In brief, a 488 nm solid state diode laser (OBIS Coherent) set at 4 mW served as the excitation source. The PL intensity was measured using a long working distance microscope objective (Mitutoyo M Plan Apo 20X, NA = 0.42, W.D. = 20 mm), band pass filtered with a 500 nm cutoff and fiber coupling into a monochromator (Princeton Instruments Acton SP2150), CCD detector (Princeton Instruments PIXIS 256) unit. The integration time was fixed at 500 ms and spectra were collected continuously over the course of the temperature ramp.

Results

Differential Scanning Calorimetry (DSC)

Figure 2 illustrates DSC traces for pristine BQR subject to successive cooling and heating cycles. The first heating trace is a signature of the as-cast morphology of BQR, which was drop-cast into the sample pan from chloroform at an elevated temperature (50 °C). The observable melting peak for the first heating trace is sharper and shifted to higher *T* than all subsequent melting peaks suggesting the solution-cast BQR has fewer, larger crystals than melt-crystallized BQR. In general, the thermal behavior matches previous DSC results for BQR, which showed three distinct transitions on cooling and a single melting peak.[10] The exotherms initiating at 191 °C and 182 °C were previously established as liquid crystalline transitions using polarized optical microscopy (POM), respectively referred to as LC_1 and LC_2. The absence of cooling rate dependence for LC_1 and LC_2 (Figure 2) corroborates the original assumption of liquid crystallinity; liquid crystal transitions are not kinetic and exhibit little to no superheating or supercooling.[19,20] The last exotherm upon cooling shows a strong cooling rate dependence with an onset temperature of 171 °C, 172 °C, and 175 °C for the transition when cooled at 10 °C/min, 5 °C/min, and 1 °C/min, respectively. This kinetic effect is a signature of crystallization, thus the third transition is to a three-dimensional ordered crystal referred to as C_{3D}. In each subsequent heating scan the melting behavior appears unaffected by the cooling rate.

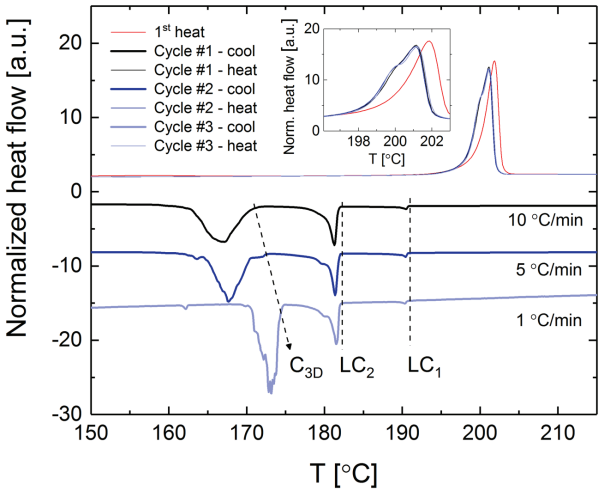

Figure 2. DSC traces of BQR melting and re-crystallization. The first heating scan is from the melting of the initial drop-cast BQR. After a 1 min isothermal hold at 215 °C, the BQR is cycled at progressively slower cooling rates (10 °C/min, 5 °C/min, 1 °C/min). Each cooling scan is followed by a heating scan, cycling between 0 °C and 215 °C. All heating scans are performed at 10 °C/min. Inset: heating scans in the region of melting. Cooling curves are displaced for clarity. Heat flow is normalized by sample mass m and cooling/heating rate β. Exotherm direction is down.

$PC_{71}BM$ loading series

Figure 3(a) illustrates the effect of $PC_{71}BM$ loading in BQR. In striking contrast to the neat material, the DSC cooling traces for BQR:$PC_{71}BM$ blends exhibit a *single* transition when $PC_{71}BM$ loading is greater than 10 % by mass. The exotherm shifts to higher temperatures at progressively slower cooling rates (data not shown) implying the transition is kinetic and thus a transition to C_{3D}. The fullerene does not, however, modify the extent of crystallization in the BQR fraction; the aggregate enthalpy change scales linearly with $PC_{71}BM$ loading through the entire

range. The exothermic signature for LC_2 is present only in the limit of low $PC_{71}BM$ loading. LC_2 formation is gradually depressed with increasing $PC_{71}BM$ loading, appears as a high temperature shoulder of the crystallization transition for the 90:10 BQR:$PC_{71}BM$ DSC trace and is absent at all higher loadings. The signature for LC_1 is undetected at all $PC_{71}BM$ loadings.

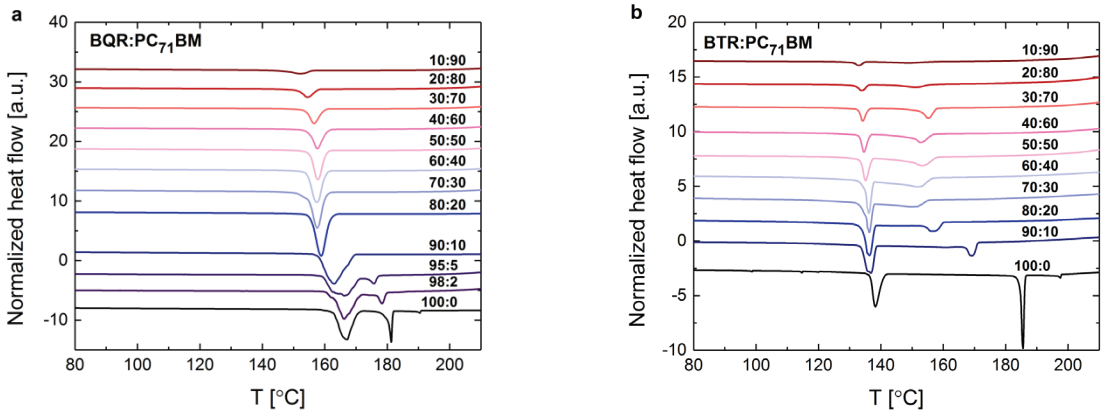

Figure 3. Typical DSC cooling traces for (a) BQR:$PC_{71}BM$ and (b) BTR:$PC_{71}BM$ blends. Heat flow is normalized by sample mass m and cooling rate β = 10 °C/min. Exotherm direction is down.

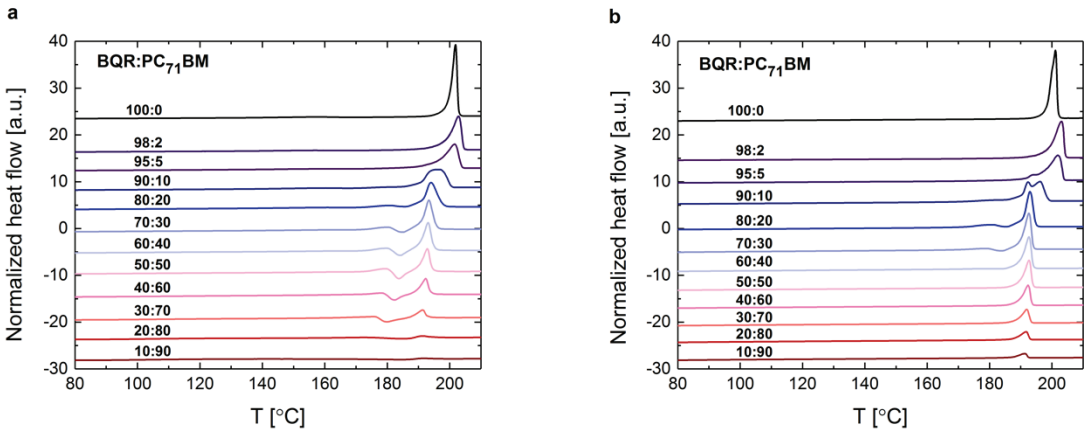

Figure 4. Typical DSC heating traces for BQR:$PC_{71}BM$ (a) on 1st heat (as-cast morphology) and (b) on 2nd heat. Heat flow is normalized by sample mass m and heating rate β = 10 °C/min. Exotherm direction is down.

The onset crystallization temperature for C_{3D} of BQR is shifted lower by up to 10 °C with increasing $PC_{71}BM$ loading. The effect is likely a consequence of freezing point depression for a miscible mixture of two components. Melting point depression has the same physical origin and can be observed for the BQR melting peak on both 1st and 2nd heat (Figure 4). Note that there are two observable melting peaks in the 1st heat DSC scans for BQR:$PC_{71}BM$ blends. The high temperature peak is attributed to C_{3D} melting. The low temperature peak, between 175 °C and 180 °C, is close to the onset temperature for LC_2 on cooling (182 °C) suggesting the presence of LC_2 in the drop-cast sample. An additional feature of the 1st heat DSC traces is an exothermic transition that immediately precedes the final BQR melting transition and grows more pronounced at higher $PC_{71}BM$ loadings. Scattering measurements (shown later) indicate the transition is a signature of $PC_{71}BM$ crystallization. A set of 1st heat DSC scans of the 50:50 BQR:$PC_{71}BM$ blend at progressively slower heating rates demonstrates that the transition is strongly kinetic and also suggest $PC_{71}BM$ cold crystallization (Figure S1); the peak transition temperature shifts from 186 °C when heated at 10 °C/min to 181 °C and 168 °C when heated at 5 °C/min and 1 °C/min, respectively. $PC_{71}BM$ is typically trapped in an amorphous, glassy state when deposited from solution in an OPV blend.[21,22] While crystallization is possible below the glass transition temperature, it does not proceed at appreciable rates until the temperature is raised above T_g that has been estimated to be ≈ 168 °C for $PC_{71}BM$.[23] Fullerene cold crystallization at $T < T_g$ of pure $PC_{71}BM$ is only possible if the blend T_g is reduced.

Like BQR, pristine BTR shows three transitions on cooling,[4,10] the first two of which are liquid crystalline (LC_1 onset at 198 °C, LC_2 onset at 187 °C) and the third is crystalline (C_{3D} onset at 142 °C). Figure 3(b) illustrates the effect of $PC_{71}BM$ on BTR crystallization. Similar to BQR, the addition of $PC_{71}BM$ in BTR eliminates the exotherm for LC_1. LC_2 is observed in the BTR: $PC_{71}BM$ blends for the entirety of the loading series, but the onset temperature is significantly depressed from that in the pristine state. Similarly, the onset temperature for C_{3D} shifts lower with increasing $PC_{71}BM$ loading. As with BQR, the temperature shift can be assumed to arise from freezing point depression on cooling. The heating curves for BTR:$PC_{71}BM$ blends also exhibit temperature depression of the BTR phase transitions (Figure S2). Unlike in BQR, the LC melting transitions are observed in neat BTR,[10] however they are suppressed or lost entirely in the presence of $PC_{71}BM$. The suppression of the melting transitions and temperature shifts imply that BTR also forms a homogeneous mixture with $PC_{71}BM$ above the melting temperature for BTR. $PC_{71}BM$ cold crystallization is indicated by a broad exotherm above 180 °C in the 1st heat DSC traces for BTR:$PC_{71}BM$ blends for all fullerene loadings.

Flory-Huggins model

The bulk heterojunction morphology in OPV blends is a consequence of the thermodynamic driving force for phase separation between the acceptor and donor materials. Segregation of donor- and acceptor-rich phases occurs at some time during the drying process and is halted by the time the film has dried. Long term stability of the metastable, nano-phase segregated state – especially at elevated temperatures – is largely a function of the chemical miscibility between the donor and acceptor materials. The Flory-Huggins interaction parameter, χ, is a classic metric for chemical

miscibility and can be estimated from melting point depression of the crystallizable component in blended systems. For blends of BQR or BTR with $PC_{71}BM$, the necessary assumptions for Flory-Huggins theory[24] are most applicable for melting depression of the $PC_{71}BM$ crystal phase, where the BQR or BTR is molten, $T_{m,PCBM} >> T_{m,BQR} > T_{m,BTR}$. Melting point depression of BXR can also be modeled, but one must consider that $PC_{71}BM$ is partially crystalline and the relative amount of crystalline and amorphous $PC_{71}BM$ material must be determined *a priori*. Figure 5 shows the $PC_{71}BM$ peak melting temperature in blends with (a) BQR or (b) BTR estimated by DSC (peak melting temperature obtained from DSC melting curves in Figure S3). To model melting point depression with the Flory-Huggins approximation,[24] it is assumed that $PC_{71}BM$ acts as a monomeric solvent (1), i.e., the molar volume of a $PC_{71}BM$ molecule, v_1, is equivalent to the size of a lattice site, v_0. BQR/BTR is modeled as a polymeric solute (2) with total molar volume, v_2, but comprised of m subunits each with molar volume v_0 or v_1. The melting point for $PC_{71}BM$, $T_{m,1}$, is expressed as:

$$\frac{1}{T_{m,1}} - \frac{1}{T^*_{m,1}} = \frac{R}{\Delta H_1}\left[\ln(\varphi_1) + \left(1 - \frac{1}{m}\right)(1 - \varphi_1) + \chi(1 - \varphi_1)^2\right], \qquad \text{(Eq. 1)}$$

where $T^*_{m,1}$ and ΔH_1 are the melting temperature and enthalpy of formation for pure $PC_{71}BM$, φ_1 is the volume fraction of $PC_{71}BM$ and R is the gas constant. To apply the model to the melting point data, the mass fraction of $PC_{71}BM$, $x_{m,1}$, was converted to volume fraction using the relation:

$$\varphi_1 = \frac{x_{m,1}}{x_{m,1} + (1 - x_{m,1})\frac{\rho_1}{\rho_2}}, \qquad \text{(Eq. 2)}$$

where ρ_1, ρ_2 are the respective densities of $PC_{71}BM$ and BQR/BTR. The crystal densities of $PC_{71}BM$[23], BTR[4] and BQR were used in the conversion: ρ_{PCBM} = 1.58 g/cm^3, $\rho_{BTR} = \rho_{BQR}$ = 1.217 g/cm^3 (the crystal density of BQR has not been reported, but should be similar to the density of

BTR). The melting temperature and enthalpy of formation for $PC_{71}BM$ were estimated from DSC: $T^*_{m,1}$ = (323 ± 1) °C and ΔH_1 = (11 ± 1) kJ/mol (reported error is one standard deviation from the mean of replicate samples). The model was fit to the data using the remaining adjustable parameters, *m* and χ. The best fit to the data and associated parameter set is shown in Figure 5. Unsurprisingly, χ is almost identical for the binary mixtures of BQR/$PC_{71}BM$ and BTR/$PC_{71}BM$. BTR and BQR are from the same family of materials and should presumably have a similar chemical miscibility with $PC_{71}BM$. The predicted number of subunits *m* is also consistent with the relative lengths of BQR and BTR; *m* scales with the length of the BXR oligomer. An alternative estimate for *m* can be made if the species molar volumes are known using the relationship associated with the lattice model, $mv_0 = v_2$. Simply estimating the molar volumes from the molecular weights (M_{BQR} = 2360 g/mol, M_{BTR} = 2030 g/mol, M_{PCBM} = 1080 g/mol) and the crystal densities using the relationship, $v = M/\rho$, then *m* = 2.8 for BQR and *m* = 2.4 for BTR. Again, *m* scales with the length of the BXR oligomer, but more significantly, the absolute values are reasonably close to the prediction from the model fit.

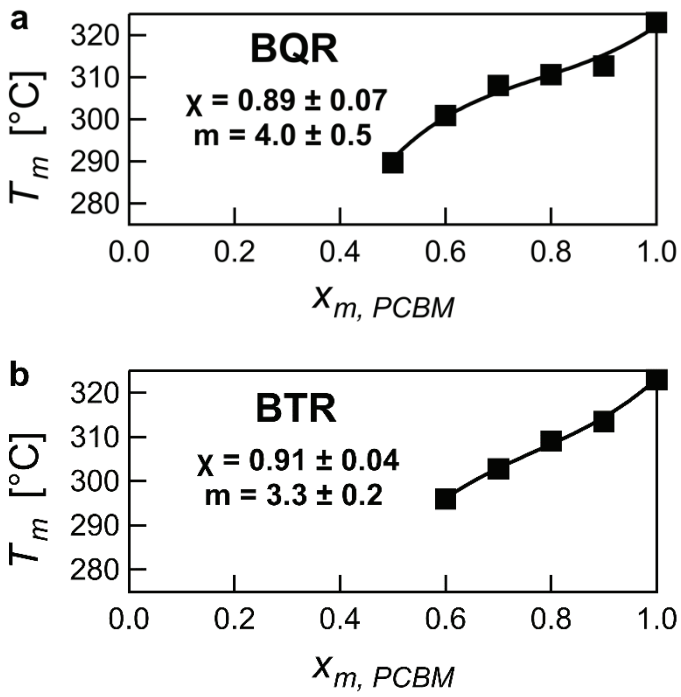

Figure 5. Crystalline melting temperature of $PC_{71}BM$ in (a) BQR and (b) BTR on 1st heat as function of mass fraction of $PC_{71}BM$. Curves are best fits to Flory's melting point depression model (see text). Error bars for melting temperature estimates (one standard deviation from the mean of replicate samples) are smaller than the size of the symbol.

Using the parameters of the Flory-Huggins model for $PC_{71}BM$ melting point depression in a blend with BXR, one can extend the model to predict a theoretical phase diagram for the crystal transitions in BXR as a function of $PC_{71}BM$ loading. The transition temperature for the oligomeric species (BQR or BTR), denoted by $T_{x,2}$ is expressed through the following relationship:

$$\frac{1}{T_{x,2}} - \frac{1}{T^*_{x,2}} = \frac{R}{\Delta H_{x,2}}[\ln(1-\varphi_1) + (1-m)\varphi_1 + \chi m(\varphi_1)^2], \qquad \text{(Eq. 3)}$$

where $T^*_{x,2}$ and $\Delta H_{x,2}$ are the peak temperature and enthalpy for a given phase transition in pure BXR. BXR transition temperatures as a function of $PC_{71}BM$ loading are modeled using the values

of m and χ determined previously in addition to the pure material transitions temperatures and enthalpies from DSC. For BQR, $\{T_{m,C_{3D}}, T_{c,LC_1}, T_{c,LC_2}, T_{c,C_{3D}}\}$ = {202 °C, 190 °C, 181 °C, 167 °C} and $\{\Delta H_{m,C_{3D}}, \Delta H_{c,LC_1}, \Delta H_{c,LC_2}, \Delta H_{c,C_{3D}}\}$ = {88 kJ/mol, 1.2 kJ/mol, 18 kJ/mol, 56 kJ/mol} and for BTR, $\{T_{m,C_{3D}}, T_{c,LC_1}, T_{c,LC_2}, T_{c,C_{3D}}\}$ = {175 °C, 198 °C, 186 °C, 138 °C} and $\{\Delta H_{m,C_{3D}}\, \Delta H_{c,LC_1}, \Delta H_{c,LC_2}, \Delta H_{c,C_{3D}}\}$ = {33 kJ/mol, 0.6 kJ/mol, 16 kJ/mol, 33 kJ/mol}. The experimental phase diagram, constructed from the transition temperatures measured by DSC (Figure 6a and 6b), is well predicted by the Flory-Huggins model; theoretical phase diagrams for BQR and BTR are reproduced in Figures 6c and 6d. Most significantly, the depression of the transition temperature is weaker for higher transition enthalpies, and by extension higher entropies. This explains the complete suppression of LC_1 at any investigated loading of $PC_{71}BM$ (>5 % by mass) in both BQR and BTR; the transition enthalpy is very weak, on the order of only 1 kJ/mol. The direct relationship between ΔH_x and transition temperature depression also explains the suppression of LC_2 in BQR. The transition enthalpy for C_{3D} is significantly greater than that for the LC_2 phase and therefore the ordering of the transitions on cooling switch with minimal $PC_{71}BM$ loading. Conversely, the difference in enthalpies between C_{3D} and LC_2 of BTR is smaller than for BQR. Suppression of LC_2 in BTR is predicted at much higher loadings of $PC_{71}BM$. LC_2 suppression in BTR, however, was not observed in DSC. Rather, transition temperatures in BTR plateau for $x_{m,PCBM} > 0.4$. Here, we recall that some fraction of $PC_{71}BM$ crystallizes on heating and remains crystalline when the DSC sample is cooled back down. This effectively traps our DSC measurements in a region of low $PC_{71}BM$ loading. Only the uncrystallized, amorphous fraction of $PC_{71}BM$ contributes to the transition temperature depression. The same effect likely holds for BQR since the transition temperatures also plateau above $x_{m,PCBM} = 0.3$.

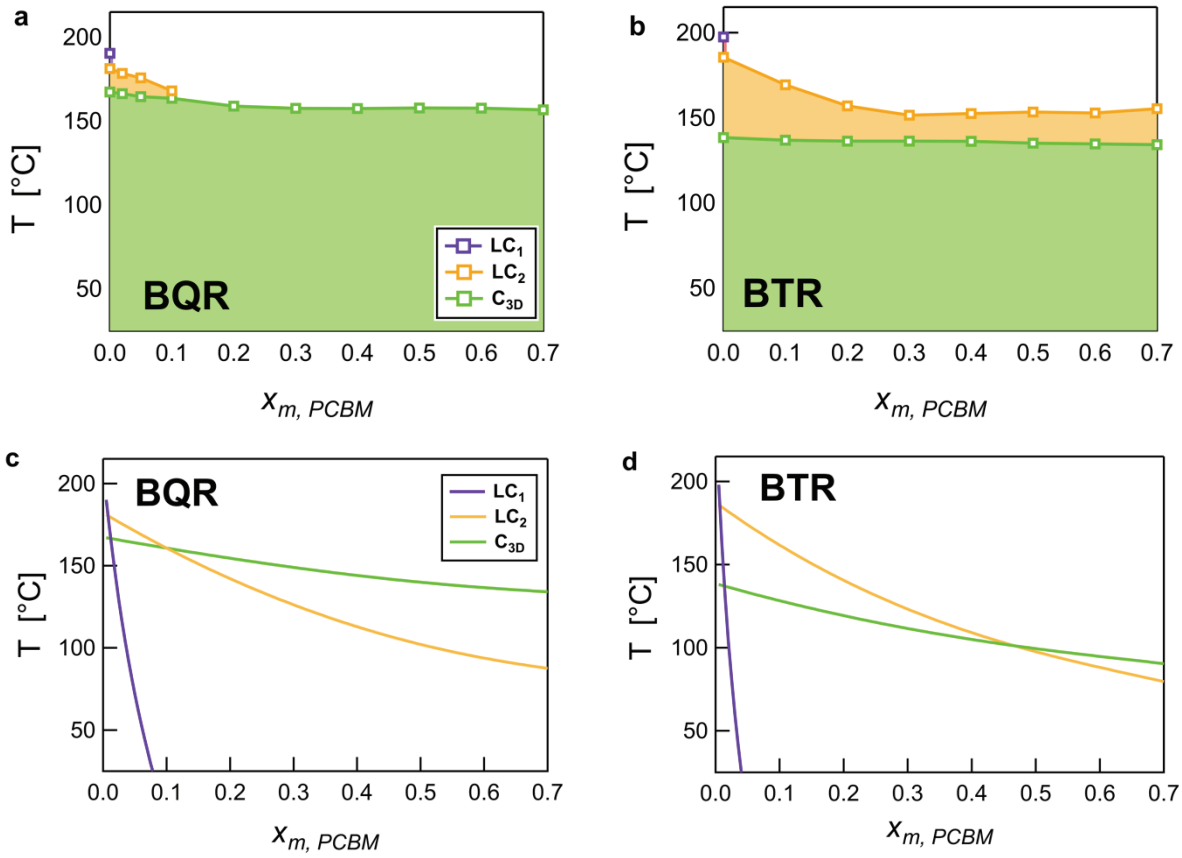

Figure 6. Phase transition temperatures in (a) BQR and (b) BTR from DSC on cooling at 10 °C/min. Theoretical phase diagrams for (c) BQR and (d) BTR as a function of $PC_{71}BM$ loading.

Device annealing

Given the strong difference in device performance between BQR and BTR with thermal annealing (TA),[10] one might expect a difference in the DSC traces on heating in the range of standard TA conditions (80 °C to 140 °C). Simply taking the DSC traces for device relevant blends (50:50 mass ratio), there do not appear to be any thermal transitions in the annealing regime for either blended system; the melting transitions begin > 140 °C. To assess if the differences arise because of prolonged thermal annealing (typically 5 min to 10 min), DSC samples were annealed at a fixed

temperature for 5 min before taking a DSC heating scan. As demonstrated by Figure 7, the most striking feature in the DSC traces following a high pre-anneal temperature (T > 140 °C for BQR and T > 90 °C for BTR) is the absence of the exothermic peak at 185 °C attributed to $PC_{71}BM$ cold crystallization. Its absence suggests $PC_{71}BM$ crystallizes during the prolonged hot stage anneal and that the annealing temperature is greater than the film's T_g. The T_g of pristine $PC_{71}BM$ is 168 °C, well above the select annealing temperatures studied, but its T_g is likely reduced in a blend with a small molecule like BQR and BTR. One can therefore attribute the difference in thermal behavior with annealing to a shift in the T_g of the blended system. Specifically, we infer that the T_g of $PC_{71}BM$ is greater than the T_g for BQR and BTR and also that BQR has a higher T_g than BTR, which is expected given the difference in chain length (BQR has an extended chromophore around the benzodithiophene core and higher melting temperature). The DSC results presented in Figure 7 provide strong evidence for the difference in device performance between thermally annealed BQR:$PC_{71}BM$ devices and BTR:$PC_{71}BM$ devices annealed at 120 °C for 10 min.[10] Specifically, $PC_{71}BM$ crystallization does not occur at any appreciable rate at this annealing condition in BQR blends, but does occur in BTR blends.

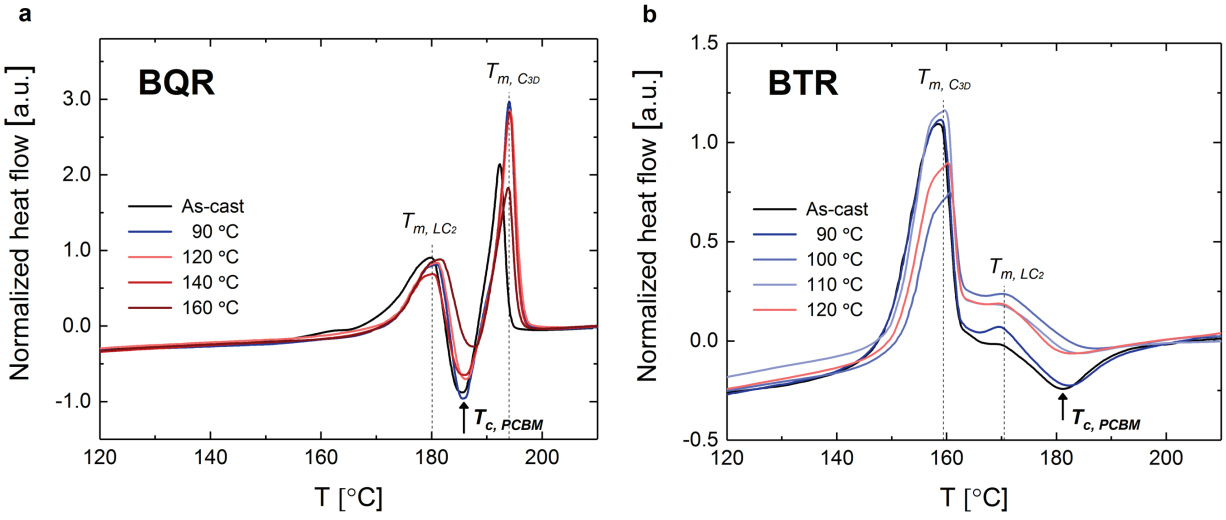

Figure 7. 1st heat DSC traces for as-cast and annealed 50:50 blends of (a) BQR:$PC_{71}BM$ and (b) BTR:$PC_{71}BM$. Curves are shifted to match the baseline heat flow in the melted state. Heat flow is normalized by sample mass m and heating rate β = 10 °C/min. The $PC_{71}BM$ cold crystallization transition is indicated. Exotherm direction is down.

Grazing incidence wide-angle X-ray scattering (GIWAXS)

In situ GIWAXS measurements provide a prospective on the development of nanoscale, crystallographic order in thin films and have proven especially valuable in understanding the effects of processing in organic electronic materials[25–27] and BHJ blends.[21,28–36] Here we use GIWAXS to probe thin films of pristine BQR and BQR:$PC_{71}BM$ blends while continuously changing temperature to directly observe the morphological features that accompany calorimetric signatures in DSC. Figure 8 summarizes the GIWAXS measurements for BQR crystallizing in a thin film from a molten state. The 2D X-ray scattering pattern for the crystalline ordered phase of

BQR (C_{3D}) is presented in Figure 8a. The crystal structure of BQR has not been reported, but if we assume BQR adopts a unit cell similar to BTR (supported by analysis in the SI), then the aromatic groups of the backbone are coplanar, molecular backbones are π-stacked with adjacent molecules and the alkyl side-chains are stacked end-to-end.[4] Following this assumption, the peak at 0.37 $Å^{-1}$ along $q_z = 0$ and the peak at -1.6 Å along $q_{xy} = 0$ collectively imply that side-chains are presented at the substrate interface in an "edge-on" crystallite orientation, the alkyl side-chain stacking distance is 17 Å and the π-stacking distance is 3.9 Å. Scattering from mixed index crystal planes is clearly observed in the 2D scattering pattern, most strongly along q_{xy} = -0.37 $Å^{-1}$ and q_{xy} = -0.56 Å.

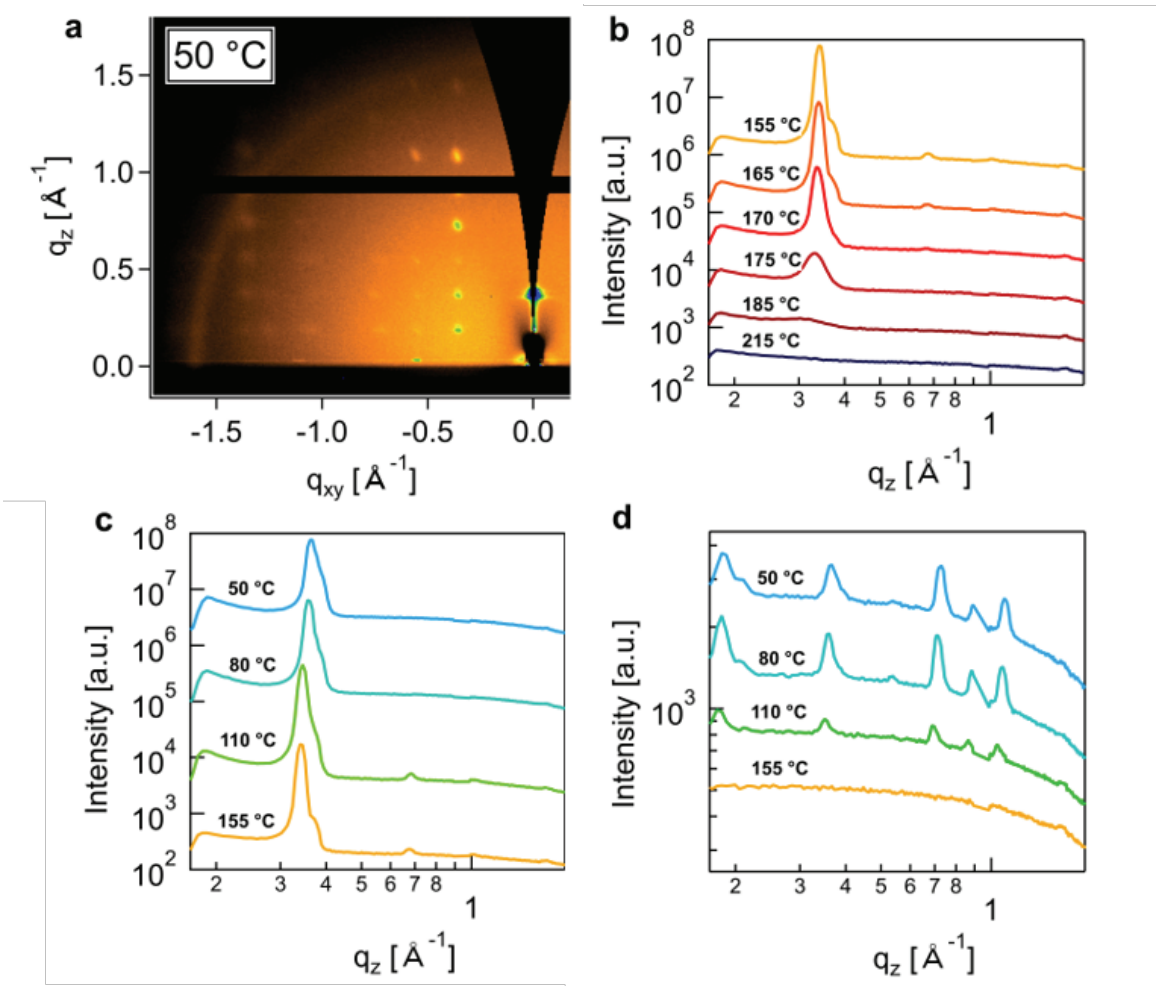

Figure 8. (a) GIWAXS detector image of pristine BQR that has been crystallized from a molten state and cooled to 50 °C. Vertical line profiles from *in situ* GIWAXS near $q_{xy} \approx 0$ are provided for pristine BQR continuously cooled from (b) the melt state at 215 °C to 155 °C and (c) 155 °C to 50 °C. (d) Corresponding vertical line profiles along q_{xy} = -0.37 Å^{-1} are also provided in the annealing regime from 155 °C to 50 °C.

Figure 8b illustrates the progression of ordering in BQR as it cools continuously from an amorphous, molten state. The material is completely isotropic with no detectable diffraction above 195 °C but once cooled to 185 °C a weak scattering feature along $q_{xy} \approx 0$ appears at a corresponding

d-spacing of approximately 20 Å. The peak is attributed to the formation of LC_1 (T_{onset} = 191 °C), which is presumed to be a locally-ordered, positionally-disordered arrangement of BQR molecules. The larger *d*-spacing compared to the primary scattering peak in C_{3D} is a consequence of thermal expansion and/or greater thermal disorder in a liquid crystalline phase. Cooling to 175 °C significantly increases the intensity of the peak and shifts the peak position to roughly 19 Å. From the DSC results, there is a transition from LC_1 to LC_2 (T_{onset} = 182 °C) over this temperature interval. Assuming that diffraction at 175 °C is a signature of LC_2 one can infer LC_2 is a denser, more ordered phase than LC_1. Upon further cooling to 170 °C the primary scattering peak continues to intensify and shift to higher q_z. By 155 °C the peak maximum is at q_z = 0.34 Å^{-1} corresponding in real space to roughly 18 Å. Two secondary features also appear in the 1D line cut along $q_{xy} \approx 0$ starting at 170 °C: a high q_z shoulder alongside the primary peak and a smaller peak centered at q_z = 0.68 Å^{-1}. From DSC, cooling at 10 °C/min initiates crystallization into the three-dimensional ordered crystal phase at 171 °C, thus we can attribute these secondary features as defining characteristics of C_{3D}. The smaller, secondary peak at q_z = 0.68 Å^{-1} is attributed to the second order diffraction of the primary peak.

Figure 8c illustrates the 1D scattering profile along $q_{xy} \approx 0$ associated with cooling the three-dimensional crystal phase of BQR to ambient temperature. There is a continuous shift in the primary peak position to larger q_z as the temperature is reduced indicating further densification of the crystal. The high q_z shoulder alongside the primary peak is maintained throughout, however the secondary peak associated with the reflection of the primary peak disappears upon cooling to 80 °C. Given the lack of any calorimetric signature from DSC, we assume the sudden loss of the peak is a consequence of signal loss from unsampled reciprocal space along the q_{xy} = 0 axis.

Specifically, we postulate that enhanced alignment of the crystallite orientation with the substrate sharpens the diffracted signal. Much of the signal is unavailable along q_{xy} = 0 axis due to the missing wedge;[27] only the breadth of the peaks along the q_{xy} = 0 axis is captured. An analysis of the polar distribution of crystallite orientations around the primary peak (Figure S4a), indicates that sharpening proceeds after cooling to 100 °C. Simultaneously, the secondary peak sharpens until it is no longer observable; the breadth of the peak completely disappears behind the missing wedge (Figure S4b). Further evidence of enhanced alignment is indicated by the appearance of the mixed index reflections at temperatures well below the onset of C_{3D} crystallization (line cuts along q_{xy} = -0.37 $Å^{-1}$ are provided in Figure 8d). Reflections first start to appear around 110 °C. No polymorphic transition is indicated in the DSC results when cooling to temperatures below 150 °C. Rather, the change is an indication of a macroscopic shift in the crystal population. A quantitative treatment of crystallinity via integration of the diffracted signal is not possible as much of the signal is lost in the missing wedge.

Diffraction from pristine BQR cast from toluene (Figure S5) suggests the crystal structure is similar to melt- crystallized BQR (Figure 8). Mixed index reflections are present in the as-cast sample (Figure S5a), but diffraction is much weaker and the spots appear blurred. The diffraction peaks sharpen as the crystal is annealed. The mixed index reflections persist up to 195 °C (Figure S5b). As clear signatures of a three-dimensional ordered phase, the scattering results confirm the peculiar stability of C_{3D} of BQR indicated by DSC; the liquid crystal transitions (LC_2 onset at 182 °C and LC_1 onset at 191 °C on cooling) are bypassed entirely on heating.

Figure 9 summarizes GIWAXS measurements from a thin film of 50:50 BQR:$PC_{71}BM$. There is a mixture of edge-on and face-on BQR crystals in the as-cast film as evidenced by the inhomogeneous arc of scattering at $q = 0.37$ Å^{-1}. Both populations of crystals remain after thermal annealing to 120 °C. Mixed index reflections in the blended film start to appear after annealing to 160 °C and disappear just before the melting temperature indicated by DSC, peak T_m = 193 °C for 50:50 BQR:$PC_{71}BM$ (Figure 9d). The area under the primary scattering peak along $q_{xy} \approx 0$ in the as-cast film is smaller compared to an annealed state (90 °C to 140 °C) implying some degree of crystallization upon annealing. Moderate thermal annealing ($T \leq 90$ °C) appears sufficient to induce crystallization of any amorphous BQR in the as-cast film since the scattered intensity effectively plateaus at higher annealing temperatures. The exact distribution of BQR phases in the blended film is unclear from GIWAXS measurements since the signatures of C_{3D} and LC_2 are relatively convolved. The high q_z shoulder in the 1D scattering profile suggests the presence of C_{3D} in the annealed film, but the lack of a shoulder does not preclude its presence in the as-cast film.

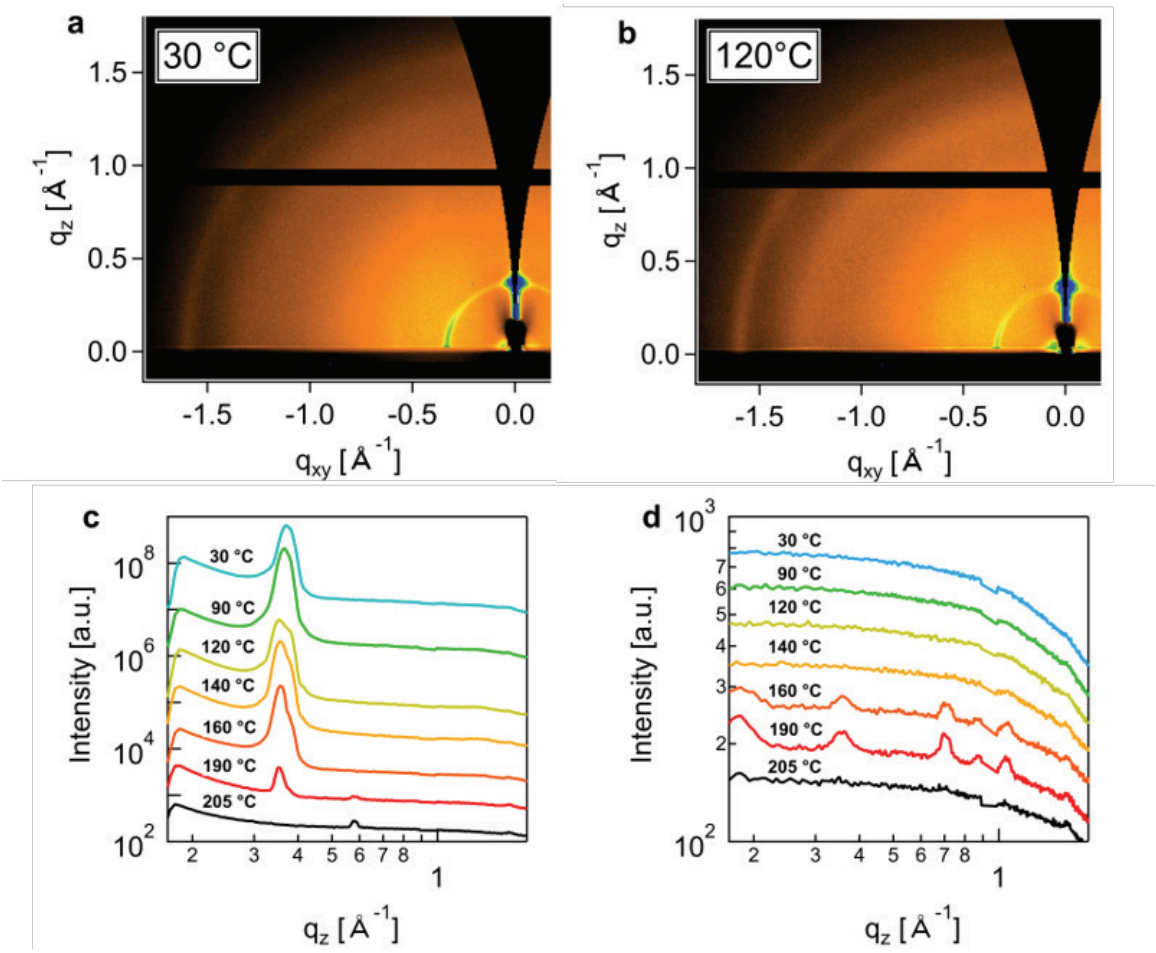

Figure 9. (a) GIWAXS detector images of a 50:50 BQR:$PC_{71}BM$ thin film blade-coated from toluene solution and (b) annealed to 120 °C. The images were collected while heating at 10 °C/min. Vertical line profiles near (c) $q_{xy} \approx 0$ and (d) q_{xy} = -0.35 Å^{-1} are also provided.

$PC_{71}BM$ crystallization in the 50:50 BQR:$PC_{71}BM$ film is indicated by a distinct scattering peak at q_z = 0.58 Å^{-1} which develops after heating above 185 °C and persists after BQR melts (Figure 9c). The peak position is consistent with scattering from pristine $PC_{71}BM$ annealed for 10 min at 180 °C.[23] The onset temperature for the scattering peak in the BQR:$PC_{71}BM$ blend matches the temperature of the exothermic signal we attributed to $PC_{71}BM$ crystallization in the 1st heat

DSC scans. The melting point of $PC_{71}BM$ is above 300 °C so one does not expect the scattering peak to disappear during *in situ* thermal cycling once it has crystallized (T_{max} = 215 °C). For all subsequent cooling and heating scans the peak at q_z = 0.58 $Å^{-1}$ remains.

Grazing incidence small-angle X-ray scattering (GISAXS)

In situ GISAXS measurements enables one to track the evolution of characteristic domain sizes and phase purity in BHJ films as a function of annealing temperature. The total scattering intensity (*TSI*) directly reflects the material purity of the donor/acceptor phases in the BHJ blends. Assuming a spatially isotropic two-phase blend, *TSI* is related to the domain composition $\varphi_{i,j}$ and the difference in scattering length density between the two phases $\Delta\rho_{i,j}$, $TSI \propto \Delta\rho_{i,j}{}^2\varphi_i\varphi_j$.[32] Estimating *TSI* from GISAXS measurements is confounded by a limited q range and reflectivity effects along q_z. Following procedures reported elsewhere,[30,32,37,38] we evaluated the total internal reflection enhanced q_{xy} data along the Yoneda axis (exact q_z range indicated in Figure 10a) hereby referred to as integrated scattering intensity (*ISI*) where $ISI \propto \int_{q_{min}}^{q_{max}} I q_{xy}^2 \, dq_{xy}$. *ISI* differs from *TSI* in that *ISI* is the integral over a finite q-range while the *TSI* is the integral over all q. Figure 10b shows the *ISI* for a BHJ blend of 50:50 BQR:$PC_{71}BM$ as it is annealed from 30 °C to 150 °C. The *ISI* is relatively constant in the low temperature regime (T < 80 °C) but increases linearly as the temperature increases. Beyond 150 °C, the *ISI* sharply decays to zero which is interpreted as a rapid increase in feature size outside of the detectable q range. The characteristic length scale or domain size reported in Figure 10c is estimated by fitting a Teubner-Strey model including a Porod background to $I(q)$.[39] The extracted long period (often interpreted as the BHJ domain size) for the

as-cast film is roughly 60 nm and remains constant upon annealing up to ≈120 °C. The peak subsequently moves towards lower absolute q_{xy} values, or larger domain sizes. The trend in *ISI* and the extracted domain size collectively suggest a nano-scale segregated morphology forms when the blend is cast from solution and that thermal annealing begins to purify the domains at temperatures above 80 °C. Domain coarsening is delayed until the temperature is increased beyond 120 °C. These GISAXS measurements directly guided annealing conditions in an analysis of OPV performance for the BQR:$PC_{71}BM$ system.

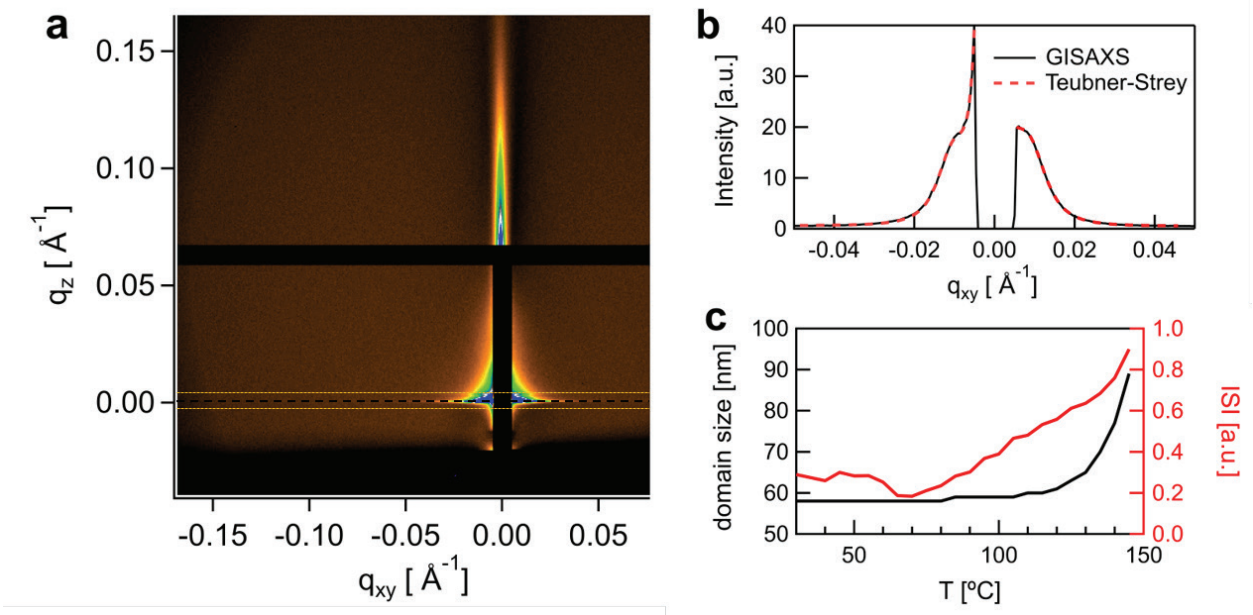

Figure 10. (a) GISAXS detector image of a 50:50 BQR:$PC_{71}BM$ blend including a representative horizontal cut at $q_z \approx 0$ from which the $I(q)$ data are extracted. (b) Teubner-Strey fit including a Porod background to $I(q)$ at 120 °C. (c) Domain size and integrated scattering intensity (*ISI*) as a function of temperature. GISAXS measurements collected *in situ* while annealing the as-cast film at 10 °C/min from 30 °C to 215 °C.

Photoluminescence spectroscopy (PL)

PL spectroscopy is capable of probing exciton separation for bulk heterojunction films.[18] In a standard OPV device, excitons created upon absorption quickly travel to a donor/acceptor interface where exciton quenching by charge separation takes place. Excitons which cannot find an interface decay and may re-emit, thus, the degree of PL quenching provides a qualitative indication of the mesoscopic morphology. Morphologies characterized by finely mixed phases quench more strongly than coarser blends. For *in situ* thermal annealing studies, PL is particularly powerful as one can track the degree of quenching in a given film over a range of annealing conditions. Figure 11 demonstrates PL quenching for a 50:50 BQR:$PC_{71}BM$ film as it is heated at 10 °C/min from 30 °C to 180 °C. The peak PL signal from the as-cast film is at 750 nm and does not shift as a function of annealing temperature. The peak intensity (Figure 10c), however, linearly decayed between 30 °C to 80 °C, then abruptly decreased to a minimum around 100 °C before exponentially increasing as the temperature continued to ramp to 180 °C.

The initial decay in PL signal is not matched by any signature in GIXD nor GISAXS. The reduction in PL intensity thus is not attributed to significant morphology changes in the BHJ, but may arise from residual solvent being driven off at the elevated temperatures. Solvent molecules in the film introduce dielectric disorder and can act as trap states, hindering charge transfer. Modest improvement in device performance has been observed in P3HT:$PC_{61}BM$ blends annealed at low temperatures (50 °C) where solvent removal is the only plausible mechanism for device improvement.[40] A sharp increase in the average domain size is indicated in both GISAXS and PL

when the 50:50 BQR:$PC_{71}BM$ film was annealed above 120 °C. In GISAXS, this "domain ripening" is interpreted from a shift in feature size to lower *q*. The *in situ* PL response corroborates this interpretation; a strong increase in PL intensity at annealing temperatures > 120 °C indicates a longer path length for exciton diffusion to a donor/acceptor boundary. We can interpret the domain ripening as a catastrophic change in the optimal device morphology which is often termed "over-coarsening".

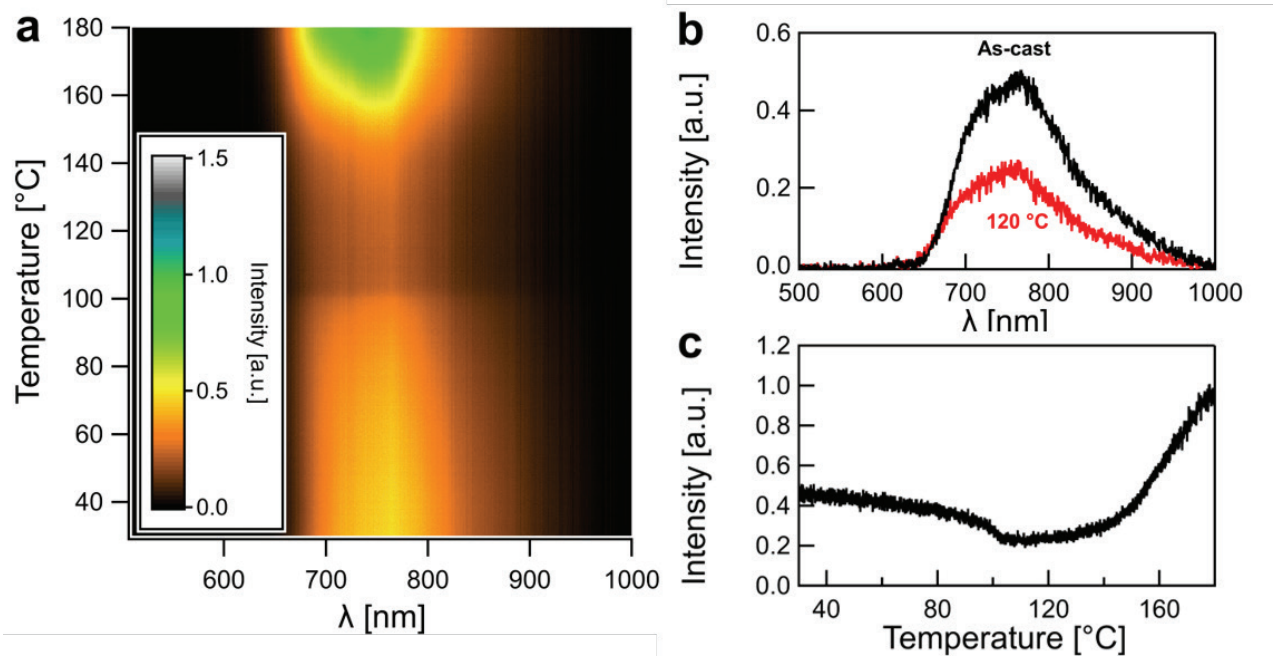

Figure 11. (a) *In situ* photoluminescence spectroscopy of a 50:50 BQR:$PC_{71}BM$ film heated at 10 °C/min. (b) Isolated PL spectra of an as-cast and annealed film. (c) *In situ* PL intensity at 750 nm as a function of stage temperature.

OPV Performance

OPV devices comprising an active layer of BQR:$PC_{71}BM$ in a 50:50 mass ratio were prepared by blade coating from toluene solution with 40 mg/mL total solids content in solution. The active layer film thicknesses were ≈ 120 nm. The as-cast devices yielded an average power conversion efficiency (PCE) around 4.7 %. Device performance peaked when annealed at 120 °C for 5 min, PCE = 7.3 %. These efficiencies are slightly lower than the performance of spun-cast devices reported by Geraghty et al: PCE = 5.3 % for the as-cast device and PCE = 8.9 % after annealing at 120 °C for 10 min.[10] In devices annealed at temperatures greater than 120 °C the short circuit current (J_{sc}), fill factor (*FF*) and *PCE* decrease monotonically with increasing temperature. The good performance of annealed, blade-coated BQR devices, relative to spun-coated, bodes well for production of small-molecule based solar cells at scale, as blade-coating has been established as a good model for continuous, slot-die deposition.

Table 1. Summary of the OPV performance for the prepared devices. The short circuit current density (J_{sc}), open circuit voltage (V_{oc}), fill factor (*FF*) and power conversion efficiency (*PCE*) represent an average of 4 devices. The uncertainties correspond to the 95 % confidence interval.

Annealing condition	$\boldsymbol{J_{sc}}$ [mA cm^{-2}]	$\boldsymbol{V_{oc}}$ [mV]	***FF*** [%]	***PCE*** [%]
As-cast	10.7 ± 0.9	954 ± 2	46 ± 1	4.7 ± 0.5
90 °C	11.3 ± 1.1	956 ± 3	47 ± 4	5.1 ± 0.9
120 °C	12.8 ± 0.6	951 ± 1	62 ± 3	7.3 ± 0.4
140 °C	9.5 ± 0.6	954 ± 4	61 ± 1	5.5 ± 0.4
150 °C	8.7 ± 0.7	947 ± 13	52 ± 1	4.3 ± 0.5
160 °C	5.9 ± 0.3	930 ± 37	38 ± 3	2.1 ± 0.2

The strong improvement in device performance at moderate annealing temperatures (90 °C to 120 °C) is likely due to domain purification. Recent studies of other BHJ systems have demonstrated a strong relationship between domain purity and the device fill factor specifically.[41,42] Here, we also see a significant increase in fill factor after annealing at 120 °C (*FF* = 62 %) compared to the as-cast device (*FF* = 46 %). GISAXS measurements of the 50:50 BQR/$PC_{71}BM$ film demonstrate an increase in *ISI* above 80 °C, which is interpreted as an increase in acceptor-/donor-rich phase purity. The domain size, however, remains fixed in this regime. Taken together, this implies molecular mobility is sufficient within domains to begin excluding impurities, but insufficient to induce large-scale morphological changes such as domain growth. Much of the improvement in domain purity may arise from changes to a mixed amorphous phase that is present in the blend in addition to BQR-rich and $PC_{71}BM$-rich domains. If present, this mixed phase of un-crystallized BQR and $PC_{71}BM$ would contribute strongly to changes on annealing, assuming the BQR crystallizes and excludes $PC_{71}BM$ from the domains. An increase in the integrated scattering intensity from GIWAXS of the 50:50 blend upon thermal annealing supports the assumption that some amount of un-crystallized BQR is present in the as-cast film.

Domain coarsening is not apparent in the blend until the film is annealed above 120 °C, as demonstrated by both GISAXS and PL spectroscopy. This correlates with a drastic drop in device performance, fill factor and short-circuit current. Based on GIWAXS and DSC measurements, coarsening is related to BQR mobility rather than $PC_{71}BM$ mobility. BQR crystals align and appear

to grow when heated above 140 °C at 10 °C/min. In this regime, however, $PC_{71}BM$ remains in a glassy state; cold crystallization does not occur until 185 °C.

Conclusions

The small molecule donor benzodithiophene-quaterthiophene-rhodanine (BQR) is an excellent candidate for large-scale OPV production using roll-to-roll printing based on its unique thermal stability and good performance (PCE > 8 %) in thick active layers (> 200 nm).[10] In this investigation we have confirmed that BQR device performance remains high when transitioning to continuous manufacture by demonstrating a blade-coated device with PCE > 7 %. Using a range of characterization techniques, we have thoroughly investigated the thermal properties of BQR in its pristine state and in blends with the fullerene acceptor $PC_{71}BM$. GISAXS and PL measurements independently suggest catastrophic changes to the mesoscopic morphology of the photoactive BQR:$PC_{71}BM$ blend when annealed above 120 °C. Device performance measurements confirm that 120 °C is the optimal annealing temperature. At this annealing condition donor/acceptor domain purification was active but the average domain size was unchanged. We attribute the superior thermal stability of BQR relative to BTR to the two additional thiophenes group in the BQR backbone. DSC results suggest that $PC_{71}BM$ mobility is suppressed more strongly in blends with BQR than in BTR, presumably resulting from a higher T_g in the BQR/$PC_{71}BM$ blend.

DSC measurements and theoretical modeling of the phase transitions in the BQR/$PC_{71}BM$ blend revealed that the liquid crystalline phases of BQR are suppressed when blended with $PC_{71}BM$. Specifically, in any device-relevant blend of BQR and $PC_{71}BM$, there is a strong preference to

form the three-dimensional ordered crystal phase of BQR. The underlying mechanism for the suppression is the interruption of the liquid crystal phase by $PC_{71}BM$; the weak association in the liquid crystal phase, quantified by the enthalpic change of the transition, is broken by the presence of $PC_{71}BM$ in the blend. Therefore, it stands to reason that most OPV materials exhibiting a liquid crystal transition in the pristine state, likely do not exhibit liquid crystallinity in a BHJ blend. Ultimately, the results of this work challenge our understanding of the role of liquid crystallinity in BHJ films for OPV applications.

Acknowledgements

A. Bourque acknowledges support from the National Institute of Standards and Technology (NIST)/National Research Council (NRC) fellowship program. S.E. acknowledges support from the U.S. Department of Commerce, NIST under the financial assistance award 70NANB17H305. A. Fuster acknowledges support from the Montgomery College/NIST Internship program. The authors would like to thank M. Heiber and A. Burns for helpful discussions in preparation of the manuscript. This work is based upon research conducted at the Cornell High Energy Synchrotron Source (CHESS) which is supported by the National Science Foundation under award DMR-1332208. Scattering data from CHESS was taken with the help of D. Smilgies.

References

(1) Søndergaard, R.; Hösel, M.; Angmo, D.; Larsen-Olsen, T. T.; Krebs, F. C. Roll-to-Roll Fabrication of Polymer Solar Cells. *Mater. Today* **2012**, *15* (1–2), 36–49.

(2) Krebs, F. C. Fabrication and Processing of Polymer Solar Cells: A Review of Printing and Coating Techniques. *Sol. Energy Mater. Sol. Cells* **2009**, *93* (4), 394–412.

(3) Wengeler, L.; Schmitt, M.; Peters, K.; Scharfer, P. Comparison of Large Scale Coating Techniques for Organic and Hybrid Films in Polymer Based Solar Cells. *Chem. Eng. Process. Process Intensif.* **2013**, *68*, 38–44.

(4) Sun, K.; Xiao, Z.; Lu, S.; Zajaczkowski, W.; Pisula, W.; Hanssen, E.; White, J. M.; Williamson, R. M.; Subbiah, J.; Ouyang, J.; et al. A Molecular Nematic Liquid Crystalline Material for High-Performance Organic Photovoltaics. *Nat. Commun.* **2015**, *6* (1), 6013.

(5) Li, W.; Hendriks, K. H.; Roelofs, W. S. C.; Kim, Y.; Wienk, M. M.; Janssen, R. A. J. Efficient Small Bandgap Polymer Solar Cells with High Fill Factors for 300 Nm Thick Films. *Adv. Mater.* **2013**, *25* (23), 3182–3186.

(6) Zeng, L.; Tang, C. W.; Chen, S. H. Effects of Active Layer Thickness and Thermal Annealing on Polythiophene: Fullerene Bulk Heterojunction Photovoltaic Devices. *Appl. Phys. Lett.* **2010**, *97* (5), 053305.

(7) Wang, N.; Chen, Z.; Wei, W.; Jiang, Z. Fluorinated Benzothiadiazole-Based Conjugated Polymers for High-Performance Polymer Solar Cells without Any Processing Additives or Post-Treatments. *J. Am. Chem. Soc.* **2013**, *135* (45), 17060–17068.

(8) Jin, Y.; Chen, Z.; Xiao, M.; Peng, J.; Fan, B.; Ying, L.; Zhang, G.; Jiang, X.-F.; Yin, Q.; Liang, Z.; et al. Thick Film Polymer Solar Cells Based on Naphtho[1,2- *c* :5,6- *c*]Bis[1,2,5]Thiadiazole Conjugated Polymers with Efficiency over 11%. *Adv. Energy Mater.* **2017**, *7* (22), 1700944.

(9) Collins, S. D.; Ran, N. A.; Heiber, M. C.; Nguyen, T.-Q. Small Is Powerful: Recent Progress in Solution-Processed Small Molecule Solar Cells. *Adv. Energy Mater.* **2017**, *7* (10), 1602242.

(10) Geraghty, P. B.; Lee, C.; Subbiah, J.; Wong, W. W. H.; Banal, J. L.; Jameel, M. A.; Smith, T. A.; Jones, D. J. High Performance P-Type Molecular Electron Donors for OPV Applications via Alkylthiophene Catenation Chromophore Extension. *Beilstein J. Org. Chem.* **2016**, *12*, 2298–2314.

(11) Müller, C. On the Glass Transition of Polymer Semiconductors and Its Impact on Polymer Solar Cell Stability. *Chem. Mater.* **2015**, *27* (8), 2740–2754.

(12) Bertho, S.; Janssen, G.; Cleij, T. J.; Conings, B.; Moons, W.; Gadisa, A.; D'Haen, J.; Goovaerts, E.; Lutsen, L.; Manca, J.; et al. Effect of Temperature on the Morphological and Photovoltaic Stability of Bulk Heterojunction Polymer:Fullerene Solar Cells. *Sol. Energy Mater. Sol. Cells* **2008**, *92* (7), 753–760.

(13) Bertho, S.; Haeldermans, I.; Swinnen, A.; Moons, W.; Martens, T.; Lutsen, L.; Vanderzande, D.; Manca, J.; Senes, A.; Bonfiglio, A. Influence of Thermal Ageing on the Stability of Polymer Bulk Heterojunction Solar Cells. *Sol. Energy Mater. Sol. Cells* **2007**, *91* (5), 385–389.

(14) Treat, N. D.; Shuttle, C. G.; Toney, M. F.; Hawker, C. J.; Chabinyc, M. L. In Situ Measurement of Power Conversion Efficiency and Molecular Ordering during Thermal Annealing in P3HT:PCBM Bulk Heterojunction Solar Cells. *J. Mater. Chem.* **2011**, *21* (39), 15224–15231.

(15) Zhao, Y.; Yuan, G.; Roche, P.; Leclerc, M. A Calorimetric Study of the Phase Transitions in Poly(3-Hexylthiophene). *Polymer (Guildf).* **1995**, *36* (11), 2211–2214.

(16) Stafford, C. M.; Roskov, K. E.; Epps, T. H.; Fasolka, M. J. Generating Thickness Gradients of Thin Polymer Films via Flow Coating. *Rev. Sci. Instrum.* **2006**, *77* (2), 023908.

(17) Ilavsky, J. Nika: Software for Two-Dimensional Data Reduction. *J. Appl. Crystallogr.* **2012**, *45* (2), 324–328.

(18) Engmann, S.; Bokel, F. A.; Ro, H. W.; DeLongchamp, D. M.; Richter, L. J. Real-Time Photoluminescence Studies of Structure Evolution in Organic Solar Cells. *Adv. Energy Mater.* **2016**, *6* (10), 1502011.

(19) Snyder, C. R.; Kline, R. J.; DeLongchamp, D. M.; Nieuwendaal, R. C.; Richter, L. J.; Heeney, M.; McCulloch, I. Classification of Semiconducting Polymeric Mesophases to Optimize Device Postprocessing. *J. Polym. Sci. Part B Polym. Phys.* **2015**, *53* (23), 1641–1653.

(20) Wunderlich, B.; Grebowicz, J. Thermotropic Mesophases and Mesophase Transitions of Linear, Flexible Macromolecules; Springer, Berlin, Heidelberg, 1984; pp 1–59.

(21) Verploegen, E.; Mondal, R.; Bettinger, C. J.; Sok, S.; Toney, M. F.; Bao, Z. Effects of Thermal Annealing Upon the Morphology of Polymer-Fullerene Blends. *Adv. Funct. Mater.* **2010**, *20* (20), 3519–3529.

(22) Westacott, P.; Treat, N. D.; Martin, J.; Bannock, J. H.; de Mello, J. C.; Chabinyc, M.; Sieval, A. B.; Michels, J. J.; Stingelin, N. Origin of Fullerene-Induced Vitrification of Fullerene:Donor Polymer Photovoltaic Blends and Its Impact on Solar Cell Performance. *J. Mater. Chem. A* **2017**, *5* (6), 2689–2700.

(23) Leman, D.; Kelly, M. A.; Ness, S.; Engmann, S.; Herzing, A.; Snyder, C.; Ro, H. W.; Kline, R. J.; DeLongchamp, D. M.; Richter, L. J. In Situ Characterization of Polymer–Fullerene Bilayer Stability. *Macromolecules* **2015**, *48* (2), 383–392.

(24) Flory, P. J. *Principles of Polymer Chemistry*; Cornell University Press: Ithaca, New York, 1953.

(25) Li, Y.; Wan, J.; Smilgies, D.-M.; Bouffard, N.; Sun, R.; Headrick, R. L. Nucleation and Strain-Stabilization during Organic Semiconductor Thin Film Deposition. *Sci. Rep.* **2016**, *6* (1), 32620.

(26) Ullah Khan, H.; Li, R.; Ren, Y.; Chen, L.; Payne, M. M.; Bhansali, U. S.; Smilgies, D.-M.; Anthony, J. E.; Amassian, A. Solvent Vapor Annealing in the Molecular Regime Drastically Improves Carrier Transport in Small-Molecule Thin-Film Transistors. *ACS Appl. Mater. Interfaces* **2013**, *5* (7), 2325–2330.

(27) Richter, L. J.; DeLongchamp, D. M.; Amassian, A. Morphology Development in Solution-Processed Functional Organic Blend Films: An In Situ Viewpoint. *Chem. Rev.* **2017**, *117* (9), 6332–6366.

(28) Richter, L. J.; DeLongchamp, D. M.; Amassian, A. Morphology Development in

Solution-Processed Functional Organic Blend Films: An In Situ Viewpoint. *Chem. Rev.* **2017**, *117* (9), 6332–6366.

(29) Engmann, S.; Ro, H. W.; Herzing, A.; Snyder, C. R.; Richter, L. J.; Geraghty, P. B.; Jones, D. J. Film Morphology Evolution during Solvent Vapor Annealing of Highly Efficient Small Molecule Donor/Acceptor Blends. *J. Mater. Chem. A* **2016**, *4* (40), 15511–15521.

(30) Engmann, S.; Bokel, F. A.; Herzing, A. A.; Ro, H. W.; Girotto, C.; Caputo, B.; Hoven, C. V.; Schaible, E.; Hexemer, A.; DeLongchamp, D. M.; et al. Real-Time X-Ray Scattering Studies of Film Evolution in High Performing Small-Molecule–fullerene Organic Solar Cells. *J. Mater. Chem. A* **2015**, *3* (16), 8764–8771.

(31) Abdelsamie, M.; Treat, N. D.; Zhao, K.; McDowell, C.; Burgers, M. A.; Li, R.; Smilgies, D.-M.; Stingelin, N.; Bazan, G. C.; Amassian, A. Toward Additive-Free Small-Molecule Organic Solar Cells: Roles of the Donor Crystallization Pathway and Dynamics. *Adv. Mater.* **2015**, *27* (45), 7285–7292.

(32) Richter, L. J.; DeLongchamp, D. M.; Bokel, F. A.; Engmann, S.; Chou, K. W.; Amassian, A.; Schaible, E.; Hexemer, A. In Situ Morphology Studies of the Mechanism for Solution Additive Effects on the Formation of Bulk Heterojunction Films. *Adv. Energy Mater.* **2015**, *5* (3), 1400975.

(33) Pearson, A. J.; Wang, T.; Dunbar, A. D. F.; Yi, H.; Watters, D. C.; Coles, D. M.; Staniec, P. A.; Iraqi, A.; Jones, R. A. L.; Lidzey, D. G. Morphology Development in Amorphous Polymer:Fullerene Photovoltaic Blend Films During Solution Casting. *Adv. Funct. Mater.* **2014**, *24* (5), 659–667.

(34) Perez, L. A.; Chou, K. W.; Love, J. A.; van der Poll, T. S.; Smilgies, D.-M.; Nguyen, T.-Q.; Kramer, E. J.; Amassian, A.; Bazan, G. C. Solvent Additive Effects on Small Molecule Crystallization in Bulk Heterojunction Solar Cells Probed During Spin Casting. *Adv. Mater.* **2013**, *25* (44), 6380–6384.

(35) Pearson, A. J.; Wang, T.; Lidzey, D. G. The Role of Dynamic Measurements in Correlating Structure with Optoelectronic Properties in Polymer : Fullerene Bulk-Heterojunction Solar Cells. *Reports Prog. Phys.* **2013**, *76* (2), 022501.

(36) Schmidt-Hansberg, B.; Sanyal, M.; Klein, M. F. G.; Pfaff, M.; Schnabel, N.; Jaiser, S.; Vorobiev, A.; Müller, E.; Colsmann, A.; Scharfer, P.; et al. Moving through the Phase Diagram: Morphology Formation in Solution Cast Polymer–Fullerene Blend Films for Organic Solar Cells. *ACS Nano* **2011**, *5* (11), 8579–8590.

(37) Pröller, S.; Liu, F.; Zhu, C.; Wang, C.; Russell, T. P.; Hexemer, A.; Müller-Buschbaum, P.; Herzig, E. M. Following the Morphology Formation In Situ in Printed Active Layers for Organic Solar Cells. *Adv. Energy Mater.* **2016**, *6* (1), 1501580.

(38) Kozub, D. R.; Vakhshouri, K.; Orme, L. M.; Wang, C.; Hexemer, A.; Gomez, E. D. Polymer Crystallization of Partially Miscible Polythiophene/Fullerene Mixtures Controls Morphology. *Macromolecules* **2011**, *44* (14), 5722–5726.

(39) Teubner, M.; Strey, R. Origin of the Scattering Peak in Microemulsions. *J. Chem. Phys.*

1987, *87* (5), 3195–3200.

(40) Wang, T.; Pearson, A. J.; Lidzey, D. G.; Jones, R. A. L. Evolution of Structure, Optoelectronic Properties, and Device Performance of Polythiophene:Fullerene Solar Cells During Thermal Annealing. *Adv. Funct. Mater.* **2011**, *21* (8), 1383–1390.

(41) Ro, H. W.; Downing, J. M.; Engmann, S.; Herzing, A. A.; DeLongchamp, D. M.; Richter, L. J.; Mukherjee, S.; Ade, H.; Abdelsamie, M.; Jagadamma, L. K.; et al. Morphology Changes upon Scaling a High-Efficiency, Solution-Processed Solar Cell. *Energy Environ. Sci.* **2016**, *9* (9), 2835–2846.

(42) Mukherjee, S.; Proctor, C. M.; Bazan, G. C.; Nguyen, T.-Q.; Ade, H. Significance of Average Domain Purity and Mixed Domains on the Photovoltaic Performance of High-Efficiency Solution-Processed Small-Molecule BHJ Solar Cells. *Adv. Energy Mater.* **2015**, *5* (21), 1500877.

Graphical Abstract

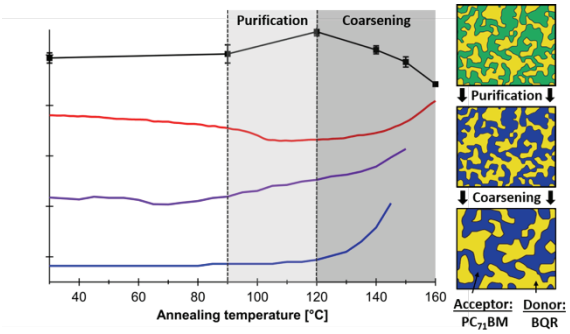

Supporting info

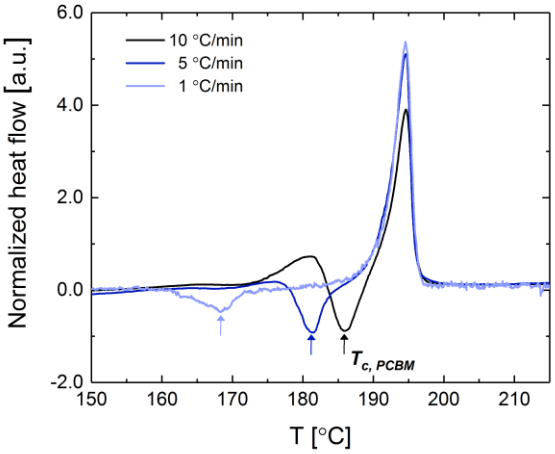

Figure S1. Typical 1st heat DSC traces for a 50:50 blend of BQR:$PC_{71}BM$ heated at 10 °C/min, 5°C/min, and 1 °C/min. Heat flow is normalized by sample mass *m* and heating rate β = 10 °C/min. Exotherm direction is down.

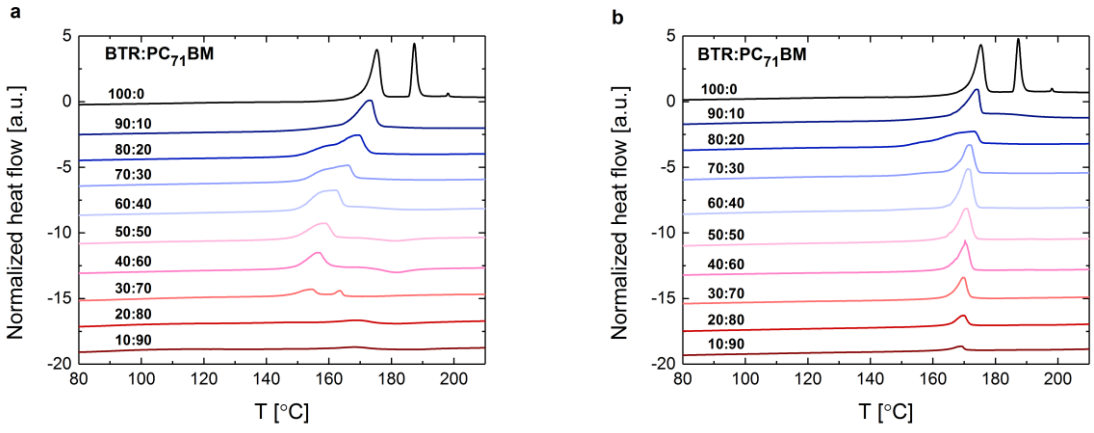

Figure S2. Typical DSC heating traces for BTR:$PC_{71}BM$ (a) on 1st heat (as-cast morphology) and (b) on 2nd heat. Heat flow is normalized by sample mass *m* and heating rate β = 10 °C/min. Exotherm direction is down.

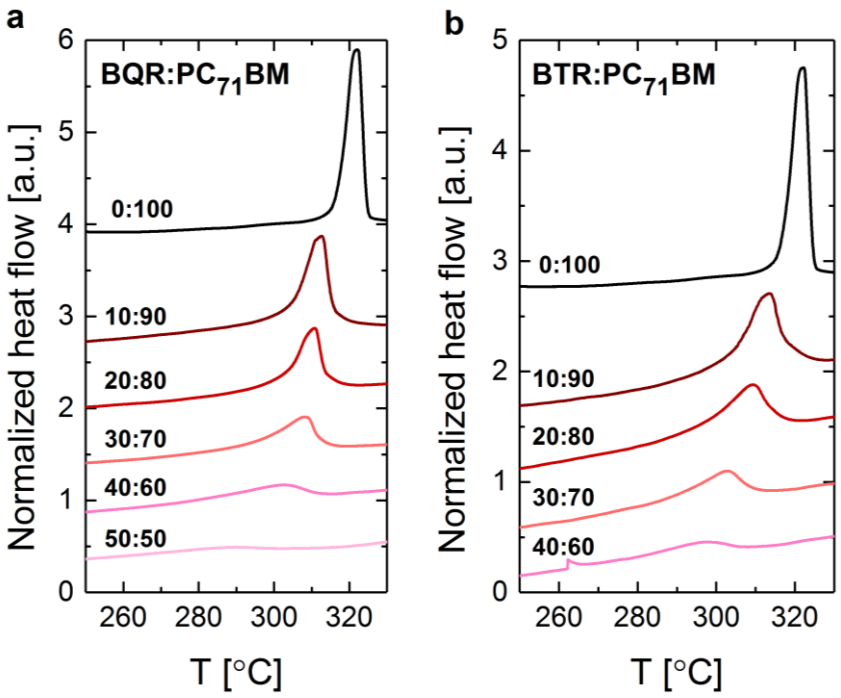

Figure S3. Typical DSC heating traces for $PC_{71}BM$ melting in (a) BQR:$PC_{71}BM$ and (b) BTR:$PC_{71}BM$ blends. Heat flow is normalized by sample mass m and cooling rate β = 10 °C/min. Exotherm direction is down.

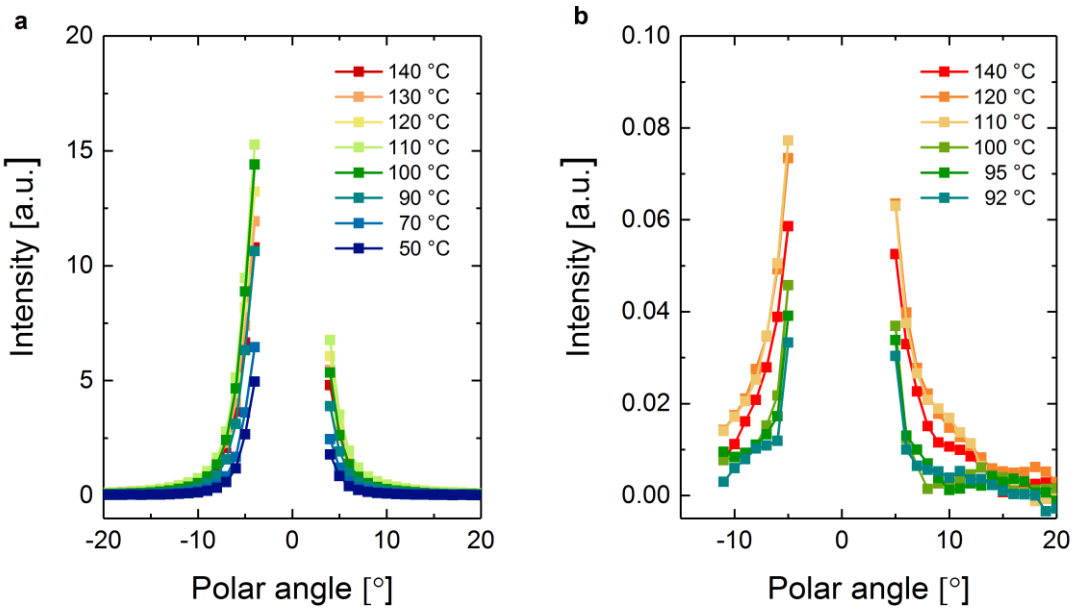

Figure S4. Extracted pole figures around (a) the primary peak ($|q| \approx 0.35$ Å^{-1}) and (b) the secondary peak ($|q| \approx 0.7$ Å^{-1}) in the GIWAXS pattern as a function of temperature upon cooling the BQR crystal at 10 °C/min.

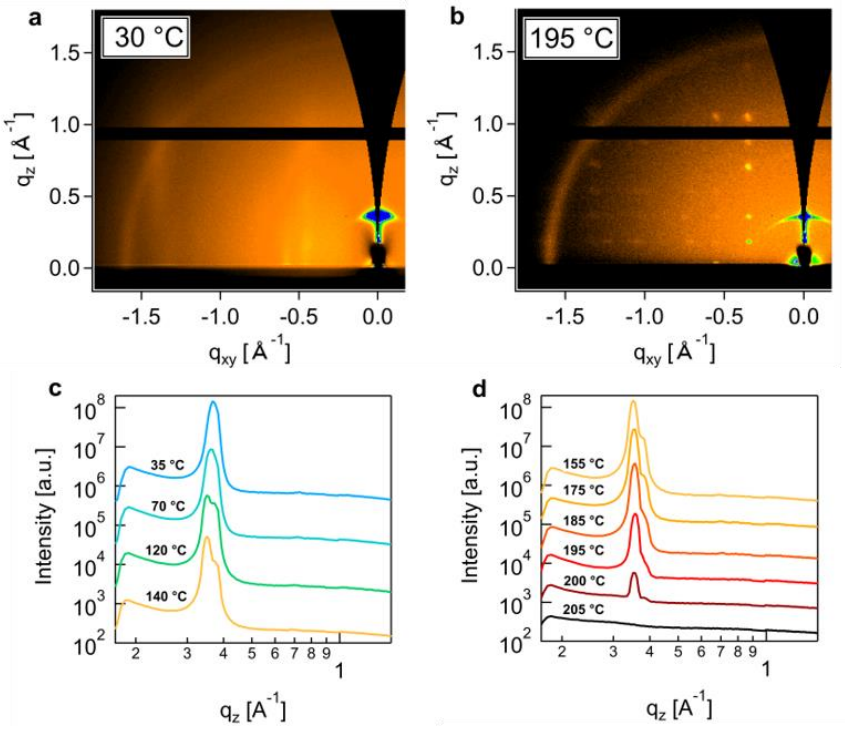

Figure S5. (a-b) GIWAXS detector images of a pristine BQR thin film blade-coated from toluene solution and annealed to the temperature specified in the figure. The images were collected while heating at 10 °C/min. (c-d) Vertical line profiles near $q_{xy} \approx 0$ are also provided.

Unit cell prediction

Upon reheating, the quiescently-cooled, pristine BQR exhibits signs of enhanced alignment indicated by sharper and more numerous high index reflections in the GIWAXS pattern. The unit cell lattice parameters for BQR were estimated from an annealed sample, reheated to 150 °C, using the Diffraction Pattern Calculator (DPC) toolkit[1] to best match the GIWAXS pattern. The contrast in the detector image and feature detection limits were adjusted manually to selectively identify relevant peaks from the local background intensity. Additionally, the extraneous intensity from main-beam bleeding over the beam stop was masked. The resulting experimental diffraction

pattern is reproduced in Figure S6a. The DPC software produces a prediction for the lattice constants by optimizing the convergence of this experimental diffraction pattern with a calculated diffraction pattern. Figure S6b displays the theoretical GIWAXS pattern at optimum convergence with the experimental scattering pattern from pristine BQR; the predicted crystal unit cell constants are reproduced in Table S1. The DPC algorithm assumes a preferred crystallite orientation in the thin film sample from which the GIWAXS data is collected and must be specified *a priori* as input to the prediction. The unit cell prediction for BQR assumes crystallites are oriented with their (010) plane parallel to the substrate. This orientation is consistent with other conjugated, organic molecules in an "edge-on" crystallite orientation;[2] typically the (010) plane bisects the direction of π-stacking between molecular backbones exposing the alkyl side-chains at the (010) interface, which lies parallel to the substrate.

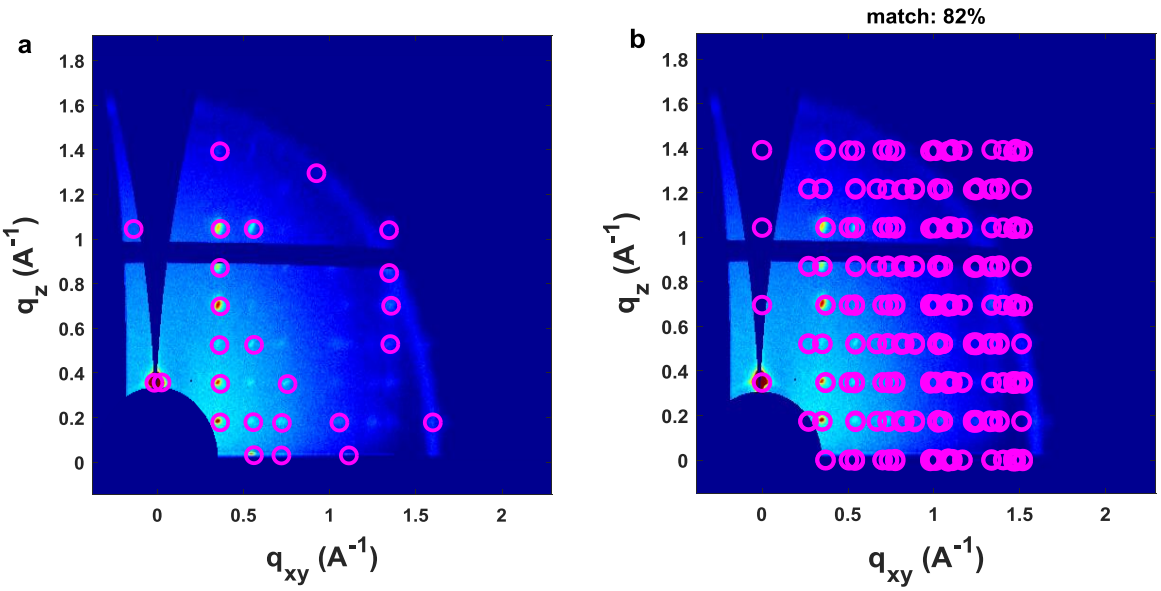

Figure S6. Experimental GIWAXS pattern for BQR that has been melted, recrystallized and reheated to 150 °C. (a) Diffraction peaks are identified from the signal background by

overlapping circles using the DPC toolkit. (b) The predicted scattering pattern for the crystal unit cell of BQR, reproduced in Table 1, with the (010) plane in contact with the surface is shown.

Table S1. Unit cell lattice parameters for BTR, previously determined by single crystal diffraction,[3] and BQR, predicted from the GIWAXS pattern assuming the (010) plane is parallel to the substrate. The sample temperature at which the measurement was performed is indicated.

Unit cell parameters	**BTR**[3]	**BQR**
T	-173 °C	150 °C
a	14.257 Å	19 Å
b	20.519 Å	22 Å
c	21.795 Å	24 Å
α	114.76 °	115 °
β	98.08 °	108 °
γ	102.00 °	105 °

It is important to note that the lattice constants for BQR in Table 1 do not constitute a unique solution for the unit cell. However, the prediction is structurally consistent with the unit cell of BTR that was determined by single crystal diffraction.[3] If one assumes BQR adopts similar crystal packing to BTR, then there should only be a shift in the crystal dimension in the direction parallel to the molecular backbone; recall that BQR is identical to BTR except for the addition of a thiophene on either side of the benzodithiophene core. The molecular backbone of BTR is orthogonal to the *b*-axis of the unit cell and effectively coincident with the <201> direction (Figure S7). Thus, the length of a BXR molecule with the structural motif of BTR can be estimated from

the lattice constants: $l_{BXR} \approx \sqrt{(2a)^2 + c^2 - (2ac)cos(\beta)}$. With the addition of two thiophene units, ≈ 4Å in length each, one expects $l_{BQR} \approx l_{BTR} + 8$ Å. Directly computing these lengths from the unit cell parameters, $l_{BTR} \approx 38$ Å and $l_{BQR} \approx 51$ Å. Accounting for thermal expansion in the BQR crystal at 150 °C in the GIWAXS sample compared to the BTR single crystal analyzed at -173°C the difference in lengths (13 Å) is entirely consistent with molecular intuition. However, we note that the GIXD estimate is not a replacement for single crystal measurements and errors on the order of several percent can be expected.

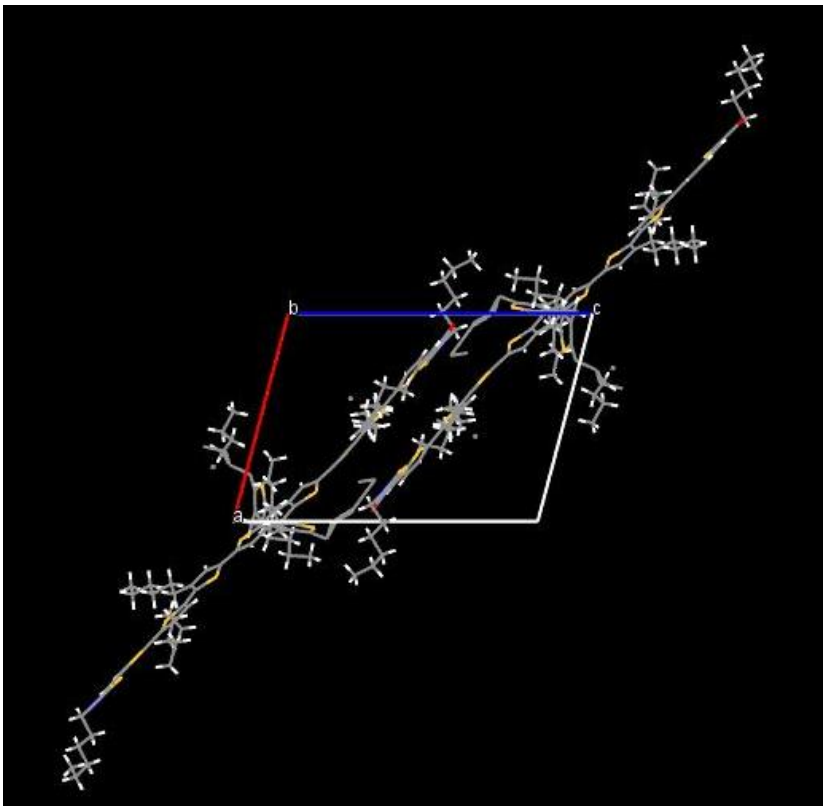

Figure S7. View down the *b*-axis of BTR.

References

(1) Hailey, A. K.; Hiszpanski, A. M.; Smilgies, D.-M.; Loo, Y.-L. The Diffraction Pattern Calculator (DPC) Toolkit: A User-Friendly Approach to Unit-Cell Lattice Parameter Identification of Two-Dimensional Grazing-Incidence Wide-Angle X-Ray Scattering Data. *J. Appl. Crystallogr.* **2014**, *47* (Pt 6), 2090–2099.

(2) Müller-Buschbaum, P. The Active Layer Morphology of Organic Solar Cells Probed with Grazing Incidence Scattering Techniques. *Adv. Mater.* **2014**, *26* (46), 7692–7709.

(3) Sun, K.; Xiao, Z.; Lu, S.; Zajaczkowski, W.; Pisula, W.; Hanssen, E.; White, J. M.; Williamson, R. M.; Subbiah, J.; Ouyang, J.; et al. A Molecular Nematic Liquid Crystalline Material for High-Performance Organic Photovoltaics. *Nat. Commun.* **2015**, *6* (1), 6013.